SIAM J. Applied Dynamical Systems
Vol. 9, No. 3, pp. 704–733

To Snake or Not to Snake in the Planar Swift–Hohenberg Equation*

Daniele Avitabile†, David J. B. Lloyd‡, John Burke§, Edgar Knobloch¶, and Björn Sandstede‖

Abstract. We investigate the bifurcation structure of stationary localized patterns of the two-dimensional Swift–Hohenberg equation on an infinitely long cylinder and on the plane. On cylinders, we find localized roll, square, and stripe patches that exhibit snaking and nonsnaking behavior on the same bifurcation branch. Some of these patterns snake between four saddle-node limits; in this case, recent analytical results predict the existence of a rich bifurcation structure to asymmetric solutions, and we trace out these branches and the PDE spectra along these branches. On the plane, we study the bifurcation structure of fully localized roll structures, which are often referred to as worms. In all the above cases, we use geometric ideas and spatial-dynamics techniques to explain the phenomena that we encounter.

Key words. Swift–Hohenberg, planar patterns, snaking, localized structures

AMS subject classifications. 37C29, 35B32, 37K50

DOI. 10.1137/100782747

1. Introduction.

Stationary spatially localized patterns are of great interest to both experimentalists and theorists [15, 34]. Such structures are observed in reaction-diffusion systems [29], optical systems [40, 7], electrical discharges [2], liquid crystals [25, 33], and even ferrofluids [36]. Related but generally time-dependent structures have been observed in several different fluid flows, including binary fluid convection [27] and plane Couette flow [42, 17]. Time-periodic localized states called oscillons were first observed in parametrically driven granular media [44] and subsequently in parametrically driven liquids [30, 1]. In many of these systems, the structures form bound states due to mutual attraction, often with an underlying hexagonal structure [2, 1, 7]; when parameters are varied, these structures may dissociate or melt [7].

All these systems are nominally homogeneous, and the localized structures form in regimes in which a spatially homogeneous trivial state coexists with a spatially structured state. Indeed, existing theory suggests that many if not all such states are associated with the presence

*Received by the editors January 19, 2010; accepted for publication (in revised form) by D. Barkley April 16, 2010; published electronically July 1, 2010.
http://www.siam.org/journals/siads/9-3/78274.html
†Department of Engineering Mathematics, University of Bristol, Bristol BS8 1TR, UK (d.avitabile@bristol.ac.uk).
The work of this author was supported by the EPSRC through the grant *Applied Nonlinear Mathematics: Making It Real* (EP/E032249/1).
‡Department of Mathematics, University of Surrey, Guildford GU2 7XH, UK (d.j.lloyd@surrey.ac.uk).
§Department of Mathematics and Statistics, Boston University, Boston, MA 02215 (jb@math.bu.edu). The work of this author was supported in part by the NSF through grant DMS-0602204.
¶Department of Physics, University of California at Berkeley, Berkeley, CA 94720 (knobloch@physics.berkeley.edu). The work of this author was supported in part by the NSF through grant DMS-0908102.
‖Division of Applied Mathematics, Brown University, Providence, RI 02912 (bjorn_sandstede@brown.edu). The work of this author was supported in part by a Royal Society–Wolfson Research Merit Award and by the NSF through grant DMS-0907904.

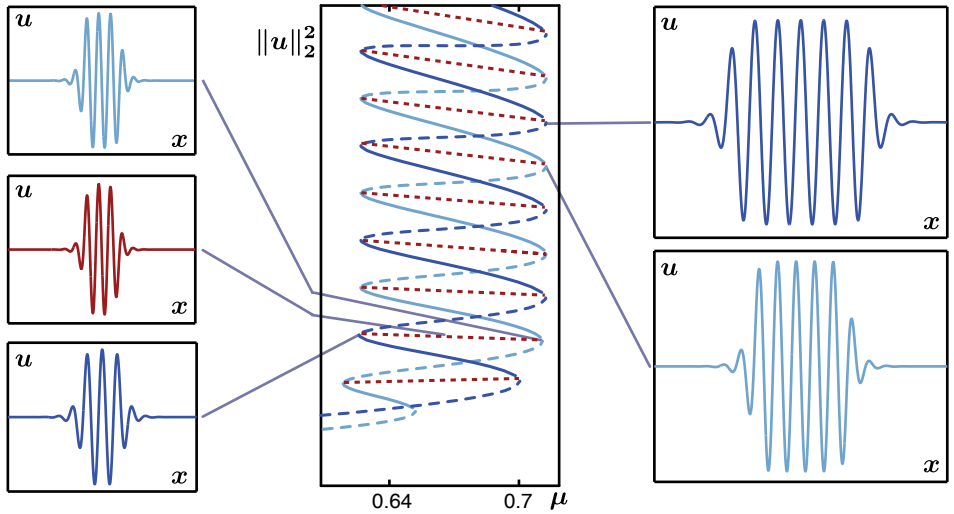

Figure 1. *Snakes-and-ladders bifurcation diagram of localized patterns of* (1.1) *for* $\nu = 2$. *The localized structures are stable along solid branches and unstable along dashed branches.*

of a subcritical Turing bifurcation, i.e., a pattern-forming instability of the trivial state. In $\mathbb{R}^2$ such a bifurcation creates localized states, in addition to regular patterns such as stripes, squares, and hexagons. Numerical continuation indicates that near this bifurcation the localized structures resemble a regular pattern with a superimposed broad slowly decaying envelope: in particular, there is no well-defined interface between the regular pattern in the interior of the localized structure and the surrounding homogeneous background state. However, in many cases this interface sharpens significantly as an appropriate parameter is varied, so that the localized structure acquires a well-defined width. With further variation of the parameter, the localized structures begin to widen in space, and it is this phenomenon, and the underlying mechanisms which cause it, that we investigate in this paper. We employ for this purpose a model equation, the Swift–Hohenberg equation,

$$u_t = -(1+\Delta)^2 u - \mu u + \nu u^3 - u^5, \qquad \mathbf{x} \in \mathbb{R}^d, \quad d = 1, 2. \tag{1.1}$$

This equation describes pattern-forming systems near instabilities with nontrivial finite spatial wavelength [22, 15] but has variational dynamics with energy

$$\mathcal{E}(u) = \int_{\mathbb{R}^d} \left[\frac{[(1+\Delta)u]^2}{2} + \frac{\mu u^2}{2} - \frac{\nu u^4}{4} + \frac{u^6}{6} \right] \mathrm{d}\mathbf{x}. \tag{1.2}$$

Local minima of $\mathcal{E}$ correspond to stable stationary solutions of (1.1). While the physical examples motivating our work are in general nonvariational, it turns out that the Swift–Hohenberg equation sheds a great deal of light on the growth of stationary spatially localized structures *in general*.

We begin by briefly summarizing the situation in one space dimension before outlining the new phenomena that we expect to encounter in two dimensions. Figure 1 shows the bifurcation diagram of stationary solutions of (1.1) on $\mathbb{R}$ computed in [8, 10, 9]. There are two intertwined

snaking branches corresponding to even and odd localized structures. As we move upwards on these branches, the localized structures widen by acquiring additional periodic rolls at an infinite number of successive fold bifurcations [45, 13]. Near each fold, the localized patterns undergo a pitchfork bifurcation at which a horizontal ladder branch of asymmetric stationary structures emerges that connects the two intertwined snaking branches. As the localized roll patterns become wider, they resemble stationary bound states of fronts that connect the homogeneous background state to a regular periodic pattern. Physically, the origin of the resulting snaking behavior can be traced to the presence of a "pinning potential" between the fronts and the periodic state between them [35]. The presence of this potential implies that the fronts will remain stationary as a parameter is varied until the energy difference between the roll state and the homogeneous background overcomes the pinning potential. In contrast, stationary fronts connecting the background to another *homogeneous* steady state are expected to exist at isolated parameter values only: in this case there is no pinning potential, and an arbitrarily small change in the parameter will cause each front to move. A "bound" state of two such fronts will therefore either expand or shrink, except at isolated parameter values.

Rephrased in dynamical systems language for the steady-state equation

$$(1+\partial_x^2)^2 u + \mu u - \nu u^3 + u^5 = 0, \qquad x \in \mathbb{R},$$

associated with (1.1), we can identify the localized roll patterns with homoclinic orbits that bifurcate from a heteroclinic cycle which corresponds to the aforementioned pair of fronts. The heteroclinic orbits in the heteroclinic cycle connect an equilibrium, corresponding to the homogeneous rest state, to a periodic orbit, which corresponds to the underlying periodic roll pattern. Thus, if we assume the existence of these fronts, we should be able to predict the snaking and ladder branches using homoclinic bifurcation theory, and such an analysis has indeed been carried out recently in [5]. For the quadratic-cubic Swift–Hohenberg equation the existence of both fronts and localized roll structures, together with their snaking scenario, has been established using a formal beyond-all-orders asymptotic analysis for (μ, ν) close to $(0, \sqrt{27/38})$ [28, 12].

We may also consider localized structures that are bound states of fronts that connect the homogeneous background state to another homogeneous state, instead of to a periodic structure. The associated spatial-dynamics scenario involves the bifurcation of homoclinic orbits from two heteroclinic orbits that connect two equilibria to each other. This scenario was investigated in [26], and the resulting bifurcation curve associated with localized structures collapses to a single asymptote in parameter space, rather than oscillating back and forth between two asymptotes. As already mentioned, this is a consequence of the absence of a pinning potential. We refer to these bifurcation diagrams as nonsnaking scenarios; see Figure 2.

The goal of this paper is twofold. First, the results in [5] suggest that snakes-and-ladders bifurcation structures can potentially be far more complicated than those found in [9] for the one-dimensional (1D) Swift–Hohenberg equation. It turns out that these more complicated scenarios occur in the planar Swift–Hohenberg equation posed on a cylinder, and we investigate the resulting patterns numerically in this paper. One particular, and perhaps surprising, finding is that asymmetric structures can be stable. Our second goal is to further elucidate the dichotomy between snaking and nonsnaking for planar structures. While the different

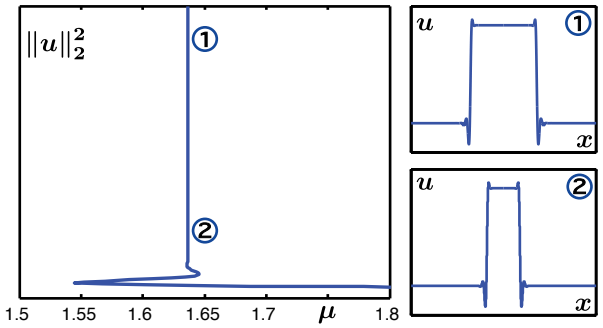

Figure 2. *Nonsnaking of localized pulses of* (1.1) *for* $\nu = 3.75$. *The broadening of the pulse is reflected in an increase of its* L^2*-norm.*

behaviors can be predicted for 1D structures using only their profiles, the distinction is more subtle for planar patterns, and it is our goal to show that it is, in general, not possible to predict whether a given pattern snakes or not by inspecting its profile.

The patterns we study on cylinders were first found in [9]: they resemble stripe patterns that evolve spatially towards spots or squares before converging to the homogeneous rest state. We also investigate fully localized stripe patterns on the plane that are often referred to as worms and present a formal spatial-dynamics argument for their bifurcation behavior. We mention that localized patterns on the plane and on cylinders were investigated in [31] by numerical continuation. In [31], it was also shown how localized patterns of the Swift–Hohenberg equation on cylinders can be captured as homoclinic orbits of an appropriate reversible Hamiltonian spatial-dynamical system.

The outline of the paper is as follows. In section 2, we set up the spatial-dynamics formulation of the Swift–Hohenberg equation and review some of the results about localized structures. The numerical algorithms we use are discussed in section 3, and we present our numerical results in sections 4 and 5. In section 6, we discuss open problems and comment on potential applications.

2. Spatial dynamics.

In this section, we consider the stationary planar Swift–Hohenberg equation

$$(1+\partial_x^2+\partial_y^2)^2 u + \mu u - \nu u^3 + u^5 = 0, \qquad (x,y) \in S^1 \times \mathbb{R}, \tag{2.1}$$

on the cylinder $S^1 \times \mathbb{R}$, where $S^1 = \mathbb{R}/2L_x\mathbb{Z}$ for some number $L_x > 0$. Equation (2.1) captures all stationary planar patterns of (1.1) that are either periodic with period $2L_x$ in the x-variable or else localized in the x-direction upon choosing $L_x \gg 1$. To explain the bifurcation structure of such patterns, which will also be localized in the y-direction, from a spatial-dynamical systems viewpoint, we write (2.1) as a first-order system in y and obtain

$$U_y = \mathcal{A}(\mu)U + \mathcal{N}(U;\nu), \qquad U = (u, u_y, u_{yy}, u_{yyy})^t \in \mathcal{X}, \tag{2.2}$$

where

$$\mathcal{A}(\mu) = \begin{pmatrix} 0 & 1 & 0 & 0 \\ 0 & 0 & 1 & 0 \\ 0 & 0 & 0 & 1 \\ -(1+\partial_x^2)^2 - \mu & 0 & -2(1+\partial_x^2) & 0 \end{pmatrix}, \qquad \mathcal{N}(U;\nu) = \begin{pmatrix} 0 \\ 0 \\ 0 \\ \nu U_1^3 - U_1^5 \end{pmatrix},$$

and $U(y)$ is, for each fixed y, a function of x that lies[1] in $H^3(S^1)\times H^2(S^1)\times H^1(S^1)\times L^2(S^1)$. From now on, we consider (2.2) as a dynamical system in the y-variable. Though (2.2) is ill-posed as an initial-value problem, the bifurcation structure of periodic, heteroclinic, and homoclinic orbits of (2.2) can be discussed and analyzed as for ordinary differential equations (ODEs), and we refer to [5, 32, 38, 39] for the relevant techniques and results.

Equation (2.2) is equivariant with respect to the $\mathbb{Z}_2$-actions

$$\rho:\ U\longmapsto -U, \qquad\qquad \tau:\ U(x)\longmapsto U(L_x-x),$$

which correspond, respectively, to the $u\mapsto -u$ and $x\mapsto L_x-x$ symmetries of (1.1). We shall see in subsection 4.2 below that the symmetry relevant for the patterns we found in our numerical explorations is the composition

$$\kappa=\rho\tau:\ U(x)\longmapsto -U(L_x-x)$$

of ρ and τ. The spatial-dynamical system (2.2) is reversible with respect to the reverser

$$\mathcal{R}:\ (U_1,U_2,U_3,U_4)^t\longmapsto (U_1,-U_2,U_3,-U_4)^t,$$

which corresponds to the reflection symmetry $y\mapsto -y$ of (1.1), and the reverser $\kappa\mathcal{R}$. We say that a solution $u(\phi,y)$ is symmetric or reversible if $\mathcal{R}u=u$ or $\kappa\mathcal{R}u=u$; otherwise, we call it asymmetric. Finally, it was shown in [31] that (2.2) admits the Hamiltonian[2]

$$\mathcal{H}(U)=\int_0^{2L_x}\left[U_2(U_4+(1+\partial_x^2)U_2)-\frac{U_3^2}{2}+\frac{[(1+\partial_x^2)U_1]^2}{2}+\frac{\mu U_1^2}{2}-\frac{\nu U_1^4}{4}+\frac{U_1^6}{6}\right]\mathrm{d}x.$$

Note that if $U=(u,0,0,0)$ is an equilibrium of (2.2), so that $u=u(x)$ is independent of y, then $\mathcal{H}(U)=\mathcal{E}(u)$, where $\mathcal{E}(u)$ is the 1D energy functional from (1.2) restricted to a periodic cell of length $2L_x$.

After these preparations, we return to the dynamical systems interpretation of the 1D patterns and their bifurcation diagrams shown in Figures 1 and 2. Schematic plots of these diagrams and the underlying solutions are given in Figures 3 and 4, now using the spatial variable y instead of x.

We begin by discussing the scenario shown in Figure 3. Assume that (2.1) admits a front $u_{\mathrm{front}}(y)$ that connects the trivial state $u=0$ to another symmetric rest state $u=\tilde{u}\in\mathbb{R}$. Fronts of this type correspond to heteroclinic orbits $U_{\mathrm{front}}(y)$ between the reversible equilibria $U=0$ and $\tilde{U}=(\tilde{u},0,0,0)$ of the dynamical system (2.2). Reversibility implies that $\mathcal{R}U_{\mathrm{front}}(y)$ is a heteroclinic orbit between $\tilde{U}$ and 0, and these two heteroclinic orbits therefore form a heteroclinic cycle. If the asymptotic rest states are both temporally stable, then they correspond to hyperbolic equilibria of (2.2). In particular, heteroclinic orbits are codimension one, and the fact that (2.2) is conservative implies that the cycle can exist only when the values of the Hamiltonian $\mathcal{H}$ evaluated at $U=0$ and $\tilde{U}$ coincide. Thus, the cycle can exist

[1]The space $H^k(S^1)$ consists of all $2L_x$-periodic functions whose first k weak derivatives are square integrable or, equivalently, for which $\sum_{k\in\mathbb{Z}}(1+k^2)|a_k|^2<\infty$, where a_k denotes the kth associated Fourier coefficient.

[2]The canonical variables are $(q_1,q_2,p_1,p_2)=(U_1,U_2,-(U_4+2(1+\partial_x^2)U_2),U_3)\in H^3(S^1)\times H^2(S^1)\times L^2(S^1)\times H^1(S^1)$ for the standard symplectic operator $\mathcal{J}$.

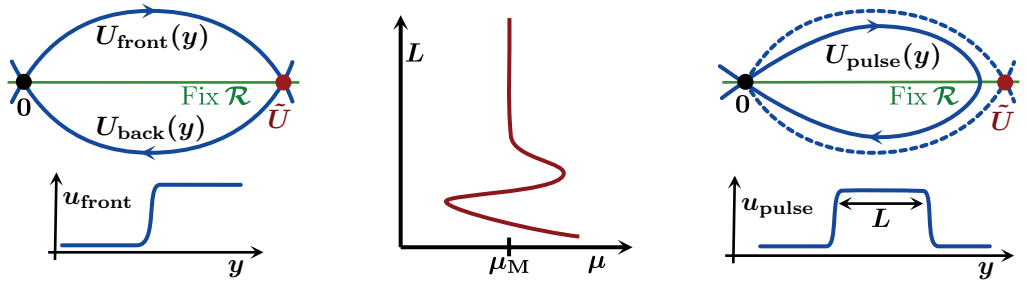

Figure 3. *Nonsnaking scenario: The left and right panels show, respectively, the initial heteroclinic cycle between the equilibria $U = 0$ and $\tilde{U}$ that corresponds to fronts and their symmetric counterparts, and the bifurcating homoclinic orbit that corresponds to pulses. The center panel illustrates the bifurcation diagram, with the L^2-norm or the width of the bifurcating pulses plotted against the bifurcation parameter μ.*

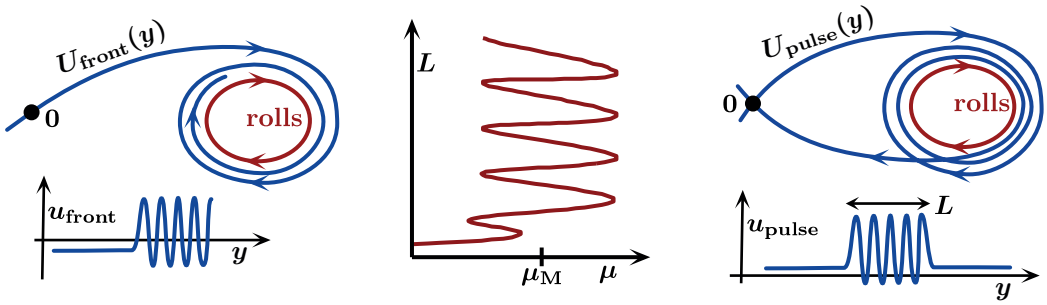

Figure 4. *Snaking scenario: The left and right panels show, respectively, a part of the initial heteroclinic cycle between the equilibrium $U = 0$ and the periodic roll pattern, and the bifurcating homoclinic orbit that corresponds to a localized roll structure. The center panel contains the bifurcation diagram, with the L^2-norm or the width of the bifurcating pulses plotted against the bifurcation parameter μ.*

only when $\mathcal{H}(\tilde{U}) = 0$. This criterion selects a parameter $\mu = \mu_{\text{M}}$, which we refer to as the Maxwell point[3] of $\tilde{U}$. As shown above, $\mathcal{H}(\tilde{U}) = \mathcal{E}(\tilde{u})$, and we therefore have $\mathcal{H}(\tilde{U}) = \mathcal{E}(\tilde{u}) = 0$ at the Maxwell point of $\tilde{U}$. In particular, we can connect two different 1D solutions by an interface in the y-direction only if their 1D energies coincide. In the ODE case, it was shown in [26] that a family of symmetric homoclinic orbits to the equilibrium $U = 0$ bifurcates from the heteroclinic orbit. The homoclinic orbits are parametrized by their width L and exist for parameters $\mu = \mu(L)$, where $\mu(L) \to \mu_{\text{M}}$ as $L \to \infty$. In particular, when plotting $\mu(L)$ against L, we obtain bifurcation diagrams such as the one found in Figure 2 or sketched in Figure 3. We remark that the Maxwell point for the nontrivial equilibrium shown in Figure 2 occurs at $\mu_{\text{M}} = 1.6367$, which gives excellent agreement with the vertical asymptote of the numerically computed bifurcation curve. Though the results in [26] are formulated for ODEs, the arguments in [32, 38, 39] imply that they also hold for (2.2).

Next, we discuss the situation shown in Figure 4, where we assume that (2.1) has a front $u_{\text{front}}(y)$ that connects the trivial state $u = 0$ to a symmetric spatially periodic roll pattern $u_{\text{rolls}}(y)$. This front corresponds to a heteroclinic orbit $U_{\text{front}}(y)$ of (2.2) that connects $U = 0$

[3]Since we consider localized structures, one of the two limiting rest states will be $U = 0$, which justifies calling μ_{M} the Maxwell point of $\tilde{U}$ and not of the pair $(0, \tilde{U})$.

to a reversible periodic orbit $U_{\rm rolls}(y)$ of the y-dynamical system. Heteroclinic orbits of this type can exist only when the Hamiltonian $\mathcal{H}$ vanishes along the periodic orbit $U_{\rm rolls}(y)$ so that $\mathcal{H}(U_{\rm rolls}(y)) = 0$ for one, and hence all, y. Periodic orbits of Hamiltonian systems come in one-parameter families that are, generically, parametrized by the value of the Hamiltonian $\mathcal{H}$. Thus, we expect that a periodic orbit $U_{\rm rolls}(y)$ with vanishing Hamiltonian exists for μ in an open interval. Furthermore, we expect that the unstable manifold of $U = 0$ intersects the stable manifold of the periodic orbit transversely inside the zero-level set of $\mathcal{H}$. Hence, heteroclinic orbits between $U = 0$ and the periodic orbit $U_{\rm rolls}(y)$ will exist over an open interval in parameter space and disappear at its end point via saddle-node bifurcations. Reversibility implies again that the heteroclinic orbit and its symmetric counterpart form a heteroclinic cycle. Homoclinic orbits that bifurcate from this cycle will correspond to localized structures that contain a long plateau where the solution resembles a spatially periodic roll pattern as sketched in Figure 4 and found in Figure 1. The results in [5] show that these homoclinic orbits will exist in the open parameter interval for which the heteroclinic cycle exists; further details of the bifurcation structure will be discussed below. We end this discussion by noting that there does not seem to be a way of predicting the existence interval of fronts. However, the variational structure of (1.1) suggests that a stationary front that connects $u = 0$ to a spatially periodic pattern may exist when the energies $\mathcal{E}$ of the two asymptotic patterns are equal. Thus, if we define the Maxwell point of a periodic pattern $u_{\rm rolls}(y)$ with $\mathcal{H}(U_{\rm rolls}(y)) = 0$ as the parameter value $\mu_{\rm M}$ for which its energy $\mathcal{E}(u_{\rm rolls})$ vanishes, then the heuristic argument given above indicates that the Maxwell point $\mu_{\rm M}$ might lie in the existence interval of fronts. This criterion turns out to be remarkably predictive: in Figure 1, for instance, the vertical asymptotes of the limiting fold bifurcations are $\mu = 0.624$ and $\mu = 0.7126$, while the Maxwell point of rolls occurs at $\mu_{\rm r} = 0.6753$.

We now briefly summarize the two scenarios described above before giving more details on the second case.

Nonsnaking scenario: Heteroclinic cycles between two reversible equilibria lead to branches of symmetric homoclinic orbits with vertical asymptote given by the Maxwell point, while asymmetric structures do not bifurcate [26]; see Figure 3.

Snaking scenario: Heteroclinic cycles between an equilibrium and a reversible periodic orbit lead to two branches of symmetric homoclinic orbits that oscillate between two distinct parameter values and to branches of asymmetric homoclinic orbits [5]; see Figure 4.

In the snaking scenario, if the heteroclinic orbits exist for $\mu = z(\varphi)$, where $\varphi \in S^1$ is the phase of the underlying periodic orbit, then it was shown in [5] that symmetric pulses that spend time $2L$ near the periodic orbit exist for the parameter value μ if and only if

$$\mu = z(L + \varphi_0) + \mathrm{O}(\mathrm{e}^{-\eta L}), \qquad L \gg 1, \qquad \varphi_0 \in \left\{0, \frac{\pi}{2}, \pi, \frac{3\pi}{2}\right\}.$$

Here, $\varphi_0 = 0, \pi$ correspond to even patterns that are $\mathcal{R}$-symmetric, so that $u(x, y) = u(x, -y)$, while $\varphi_0 = \pi/2, 3\pi/2$ correspond to odd patterns with $\kappa\mathcal{R}$-symmetry for which $u(x, y) = -u(L_x - x, -y)$; the two different possible values of φ_0 in each of the above two cases reflect the fact that we get two patterns, namely u and κu, for each fixed reverser. Exponentially close to the folds of the snaking branch, asymmetric pulses bifurcate from the symmetric

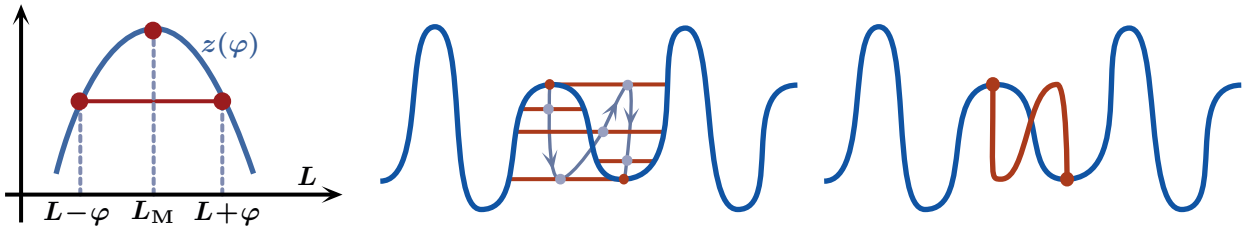

Figure 5. *Solutions (L, φ) of (2.3) are determined by the abscissas $L \pm \varphi$ of the intersection points of a fixed horizontal line segment with the graph of z. Continuing these solutions by moving the line segment up and down generates the entire bifurcation branch. If φ reaches π, the branch terminates at the second snaking curve. (Reproduced from [5].)*

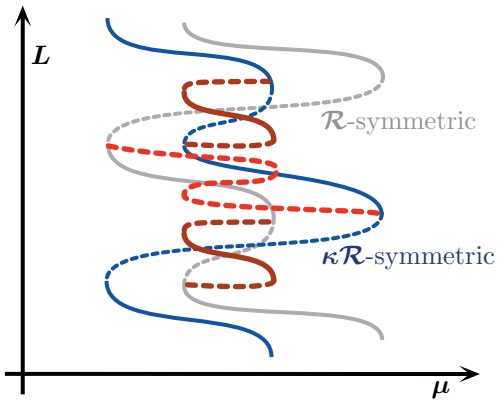

Figure 6. *The two primary snaking branches correspond, respectively, to $\mathcal{R}$- and $\kappa\mathcal{R}$-symmetric localized patterns. If these branches oscillate between four saddle-node asymptotes, then the analysis in [5] predicts the ladder branches of asymmetric pulses shown above, where reconnecting and cross-connecting ladders are shown in brown and red, respectively. The formal arguments in [5, section 7] further predict the stability and instability of solutions along the ladder branches as indicated above by solid and dashed lines, respectively.*

pulses. The associated bifurcation curves can be found by solving

$$z(L+\varphi) = z(L-\varphi) \tag{2.3}$$

for (L, φ); here $2L$ is again the time spent near the periodic orbit, while $\varphi \in [0, 2\pi]$ measures the degree of asymmetry, with integer multiples of $\pi/2$ corresponding to symmetric patterns. We refer to Figure 5 for a graphical method of computing the asymmetric ladder branches. As shown in [5], the branches emerging near global maxima and minima of z connect the bifurcation curve of even patterns with that of odd patterns (we refer to these ladder branches as cross-connecting). In contrast, the asymmetric ladder branches that bifurcate near nonglobal maxima or minima of z always begin and end at the same bifurcation curve (we refer to these ladders as self-connecting). Of particular interest to our discussion is the prediction of the ladder structure for snaking branches that snake between four saddle-node limits, which we show in Figure 6.

We note that [5, section 7] asserts that the stability properties of asymmetric ladder states can be deduced formally from the stability properties of the symmetric states: if the ladder

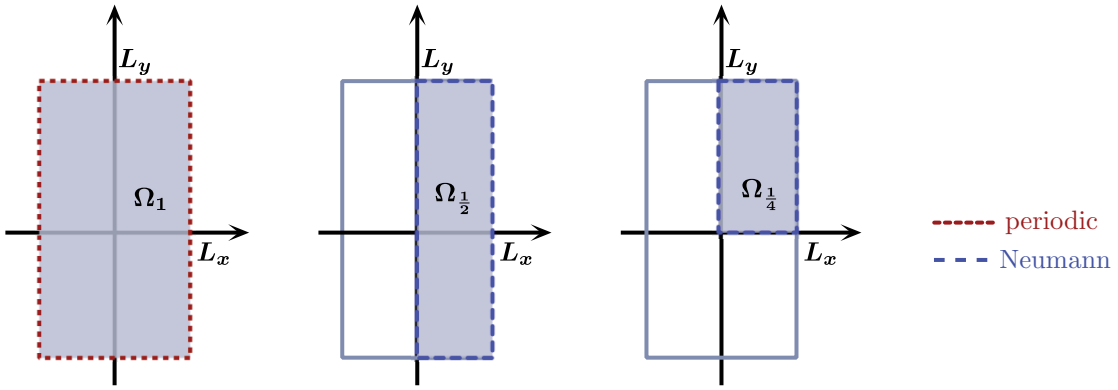

Figure 7. *Computational domains used. Left: The full cylinder domain,* $\Omega_1 = (-L_x, L_x) \times (-L_y, L_y)$. *Center: Domain* $\Omega_{\frac{1}{2}} = (0, L_x) \times (-L_y, L_y)$ *used to compute patterns that are not symmetric in the* y*-variable. Right: Domain* $\Omega_{\frac{1}{4}} = (0, L_x) \times (0, L_y)$ *used to compute patterns that are symmetric in the* y*-variable.*

state corresponds to abscissas $L \pm \varphi$, as illustrated in Figure 5, then it should be stable if and only if the two symmetric states of widths $L \pm \varphi$, respectively, that make up the asymmetric state are both stable. If the stability of the symmetric snaking pulses is as indicated in Figure 6, then the stability properties of asymmetric ladder states should be as shown in Figure 6. In subsection 4.2, we will examine the validity of this prediction numerically.

Numerically, we compute snaking branches of symmetric solutions and plot μ against the squared L^2-norm $\|u\|_2^2$ of pulses to illustrate the existence region of symmetric localized patterns. Since

$$\|u\|_2^2 \propto L + p(L) + \mathrm{O}(\mathrm{e}^{-\eta L}) \qquad \text{and} \qquad \mu = z(L + \varphi_0) + \mathrm{O}(\mathrm{e}^{-\eta L})$$

for some 2π-periodic function $p(L)$ and some $\eta > 0$, we can use the norm $\|u\|_2^2$ to predict ladder structures, provided that we are sufficiently high up on the snaking branch.

3. Numerical algorithms.

In this section, we outline the numerical algorithms that we use to compute localized patterns on cylinders and the plane. We focus on stationary solutions $u(x, y)$ of the Swift–Hohenberg equation (1.1) that are symmetric with respect to reflections in x and, in addition, either periodic or localized in the x-direction. Furthermore, we consider only solutions that are localized in the y-direction, so that $u(x, y)$ converges to zero as $|y| \to \infty$ uniformly in x. Such structures $u(x, y)$ can be found as solutions to

$$(1 + \Delta)^2 u + \mu u - \nu u^3 + u^5 = 0, \qquad (x, y) \in \Omega_{\frac{1}{2}}, \tag{3.1}$$

on the domain $\Omega_{\frac{1}{2}} = (0, L_x) \times (-L_y, L_y)$ with Neumann boundary conditions (see Figure 7(center)). Here, $L_y \gg 1$, and L_x is taken to be half the period in x if u is periodic in x or chosen to satisfy $L_x \gg 1$ if u is localized in x. Translation invariance of the Swift–Hohenberg equation on the original unbounded domain implies that any fixed translate $u(x, y + y_0)$ of a stationary solution $u(x, y)$ is also a solution. Restricting y to the bounded interval $(-L_y, L_y)$ with $L_y \gg 1$ breaks the translational symmetry. However, solutions that are localized in y will interact only weakly with the boundary, and we therefore expect that each translate

$u(x, y + y_0)$ will remain an approximate solution. In particular, the linearization about a localized structure will be close to singular, and Newton's method may not converge. To deal with this problem, we impose a phase condition that selects one specific translate from the family $u(x, y + \cdot)$ of solutions on the unbounded domain. In order to solve for this additional constraint, we exploit the fact that weak interaction with a boundary turns the formerly stationary solutions into waves that travel with a very small speed c in the y-direction. Thus, introducing the speed c as an extra parameter allows us to solve the phase constraint, and we refer to [11] for more details and a rigorous justification of this procedure. The system consisting of the phase condition and the Swift–Hohenberg equation formulated in a frame that moves with speed c in the y-direction is given by

$$(1 + \Delta)^2 u + c u_y + \mu u - \nu u^3 + u^5 = 0, \qquad (x, y) \in \Omega_{\frac{1}{2}}, \tag{3.2}$$

$$\iint_{\Omega_{\frac{1}{2}}} u_y^{\mathrm{old}} (u - u^{\mathrm{old}}) \, \mathrm{d}x \, \mathrm{d}y = 0, \tag{3.3}$$

where u^{old} is a reference solution (for instance, the initial guess or a solution computed previously for a different parameter value). The phase condition (3.3) corresponds to setting the derivative of the function $y_0 \mapsto \|u(\cdot, \cdot + y_0) - u^{\mathrm{old}}(\cdot, \cdot)\|_2^2$ at $y_0 = 0$ to zero and replacing the derivative u_y by u_y^{old}, which is justified when u is close to u^{old}; equation (3.3) therefore selects the approximate solution closest to u^{old} in the L^2-norm. The derivative of (3.2)–(3.3) with respect to (u, c) is then regular, and (3.2)–(3.3) can be solved for (u, c), with c approximately zero, using Newton's method.

The stability of a solution $u(x, y)$ of (3.1) can be determined by linearizing (3.1) about $u(x, y)$ and finding the rightmost eigenvalues of the resulting linear operator posed on $\Omega_{\frac{1}{2}}$ with Neumann boundary conditions (which is not equivalent to the stability on the full domain $\Omega_1 = (-L_x, L_x) \times (-L_y, L_y)$).

If u is reflection-symmetric in y, in addition to the other symmetries mentioned above, then we may compute it using the equation

$$(1 + \Delta)^2 u + \mu u - \nu u^3 + u^5 = 0, \qquad (x, y) \in \Omega_{\frac{1}{4}}, \tag{3.4}$$

on the domain $\Omega_{\frac{1}{4}} = (0, L_x) \times (0, L_y)$ with Neumann boundary conditions (see Figure 7(right)). In this case, the boundary condition at $y = 0$ factors out the approximate translation symmetry, and we can solve (3.4) directly using Newton's method; see [11]. Where possible, we will use this approach.

It remains to discuss how we discretize and then solve the above equations in space. We used three different programs for our computations:

1. TRILINOS/PARACONT. To solve (3.4) on large computational domains $\Omega_{\frac{1}{4}}$, we use a 13-point finite-difference stencil for the spatial discretization and solve the resulting system using the continuation framework PARACONT [3, 31], a module built on top of the package TRILINOS [21]. PARACONT makes use of the parallel solver algorithms implemented in TRILINOS, which allows us to continue localized structures such as worms on quite large domains. We used PARACONT only[4] for solutions with reflection symmetry in y on the domain $\Omega_{\frac{1}{4}}$.

[4] PARACONT now also works with phase conditions, but we implemented this feature only at a later stage.

2. AUTO07P [19]. To continue solutions of (3.2)–(3.3), we followed the strategy outlined in [31] for a slightly different setting: we discretize the circumferential variable x using a Fourier–Galerkin approximation (using only cosine functions to accommodate the Neumann conditions) and solve the resulting boundary-value problem in the remaining y-variable in AUTO07P. The advantages are that AUTO07P uses an adaptive mesh in the y-direction and runs on multiple processors; the main disadvantage is that stability computations are not possible within AUTO07P. AUTO07P's branch-switching facility failed near pitchfork bifurcations of symmetric structures. Instead, we break the $y \mapsto -y$ symmetry of the equation by adding the term $\gamma \sin(y)u$, with $0 < \gamma \ll 1$, to the right-hand side of (3.2). Adding this term breaks the pitchfork bifurcation and allows us to find asymmetric branches. In our computations, we work with $n_x = 5$ Fourier modes on the cylinder, since higher Fourier modes are found to be of order $O(10^{-7})$, and use the default values of the AUTO constants with number of mesh intervals NTST $= 400$.

3. MATLAB/EPCONT. Our third implementation allows us to solve (3.1) directly, without having to add a phase condition, and simultaneously to compute the rightmost eigenvalues of the PDE linearization to test for stability. We use a modified version of the MATLAB continuation toolbox EPCONT, a predecessor of COCO [16], developed by Schilder. This toolbox provides a general framework for continuing solutions to algebraic equations. We made two changes to EPCONT. First, we use the MATLAB Newton trust-region solver FSOLVE, which works very well for problems with singular Jacobian. Second, we projected out the approximate translation directions in each predictor step during the continuation. We discretize (3.1) using spectral differentiation matrices in the circumferential x-direction (see [43, section 3] for details) and finite differences in the y-direction. Typical mesh sizes are $n_x = 8$ Fourier modes and $n_y = 800$ equidistant points on the domain $(0, \pi) \times (-50, 50)$. The rightmost eigenvalues of the linearization of (3.1) with Neumann or Dirichlet boundary conditions are computed in MATLAB with the sparse eigenvalue solver EIGS using the shift-invert option. The shift is initialized using an a priori bound for the spectrum and then updated with the rightmost eigenvalue during continuation. We typically computed the ten rightmost eigenvalues. Stability was also checked using an initial-value problem solver.

4. Localized stripe patterns on cylinders. In this section, we consider the equation

$$(1 + \Delta)^2 u + \mu u - \nu u^3 + u^5 = 0, \qquad (x, y) \in \Omega_{\frac{1}{2}},$$

on the domain $(0, L_x) \times (-L_y, L_y)$ with Neumann boundary conditions. Unless stated otherwise, we take $\nu = 2$ throughout this section. We focus on patterns that are localized in the y-direction and both symmetric and periodic in the x-direction with period $2L_x \approx 2\pi$. Bifurcation diagrams are visualized by plotting the parameter μ against the squared L^2-norm $\|u\|_{L^2}^2$ of the underlying pattern. Patterns $u(x, y)$ are visualized by color plots, with x plotted horizontally and y vertically, where the values of $u(x, y)$ are represented by different colors as indicated in the color bars in Figures 8 and 9. In particular, red and blue correspond, respectively, to positive and negative values of u. To better visualize patterns, we duplicate their profiles several times in the periodic x-direction in all color plots. Finally, unless stated otherwise, the stability of patterns that are periodic in the x-direction with period $2L_x$ is computed on the interval $(0, L_x)$ with Neumann boundary conditions.

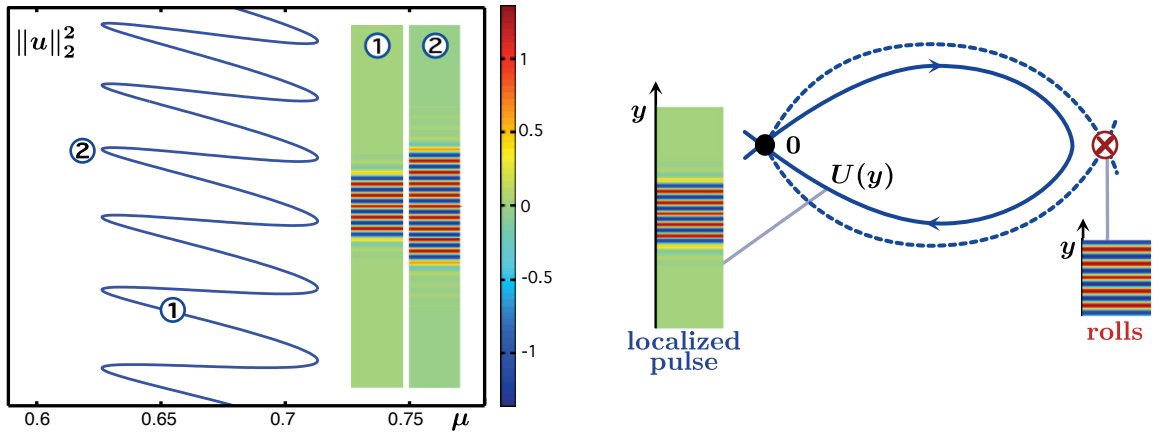

Figure 8. *The left panel contains the bifurcation diagram for snaking planar localized rolls for $\nu = 2$. The associated spatial-dynamics interpretation for the y-evolution is shown in the right panel. The roll pattern shown in the right panel corresponds to a periodic orbit in the y-dynamics: throughout this paper, we indicate equilibria of the y-dynamics by filled circles, and periodic orbits (in an appropriate Poincaré section) by circled crosses.*

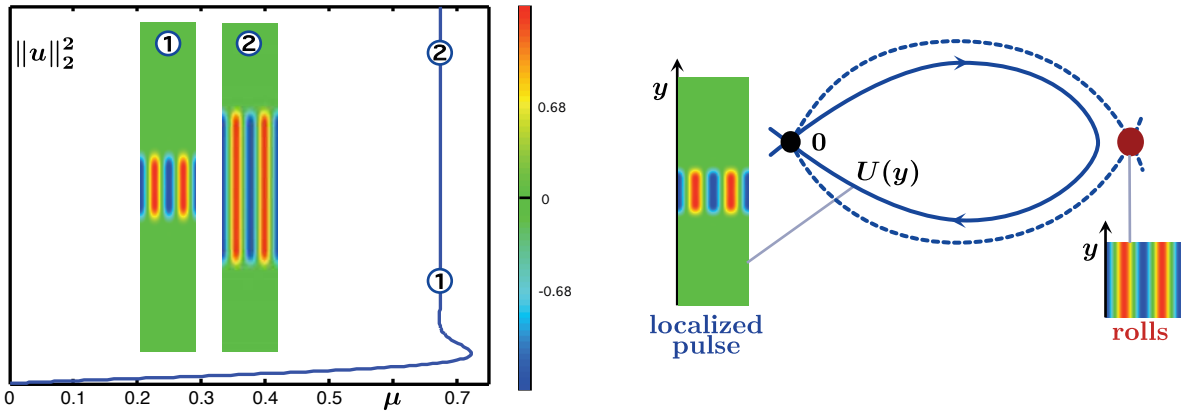

Figure 9. *Nonsnaking localized rolls for $\nu = 2$ are shown in the left panel, while the associated spatial-dynamics interpretation for their y-evolution is shown in the right panel. The roll pattern shown in the right panel corresponds to an equilibrium of the y-dynamics. (Recall that equilibria are indicated by filled circles.)*

4.1. Planar localized rolls. The 1D localized structures found in Figure 1 can be viewed as planar localized rolls. Figure 8 shows their bifurcation diagram (which is, of course, identical to those of localized 1D roll patterns) and their interpretation in terms of the spatial dynamical system (2.2) in the evolution variable y. The rolls in the interior of the localized structure are periodic in the vertical y-variable, and localized planar rolls can therefore be viewed as $\mathcal{R}$-reversible homoclinic orbits that arise near a heteroclinic cycle from the equilibrium $U = 0$ to a periodic solution that corresponds to the y-periodic roll pattern: this explains why snaking occurs. We remark that the localized rolls shown in Figure 8 are found to be alternately stable and unstable.

On the other hand, instead of orienting rolls parallel to the interface with the trivial

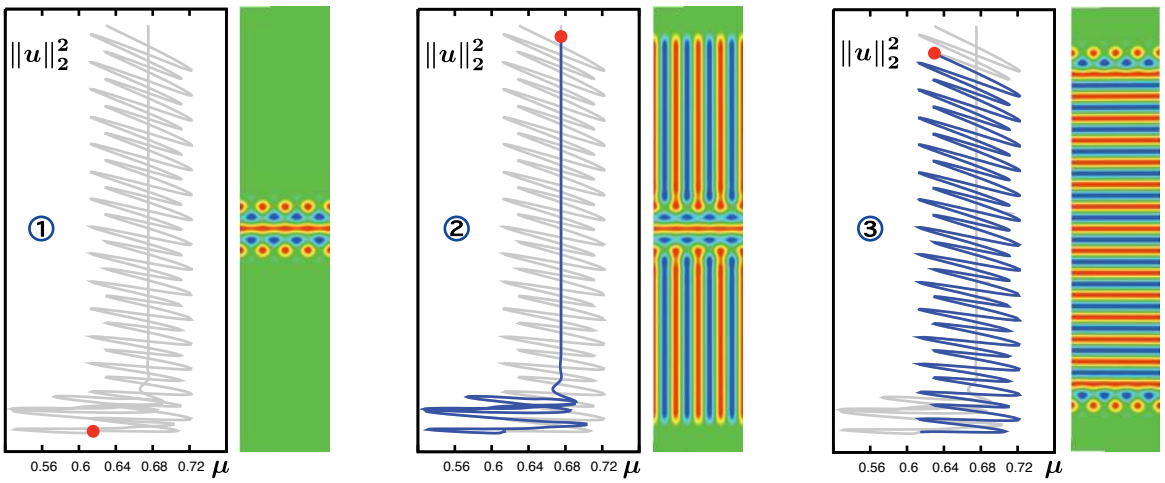

Figure 10. *Panel* 1 *contains the bifurcation diagram of an almost planar stripe pattern: the pattern profile corresponding to the red dot is shown to the right. Decreasing* μ *leads to the nonsnaking branch shown in panel* 2*. Increasing* μ*, on the other hand, leads to the snaking branch shown in panel* 3*: an interior roll section is developed which grows as we move along the branch. The family of solution profiles along the entire bifurcation curve can be viewed in the accompanying movie file* (78274_01.mpg [2.4MB])*. Solutions are computed for* $\nu = 2$ *with algorithm* 1 *on* $\Omega_{\frac{1}{4}}$ *with* $L_x = 12.6$*,* $L_y = 62.8$*,* $n_x = 33$*, and* $n_y = 129$*.*

state as in the case of Figure 8, we may seek localized roll structures for which the rolls are oriented perpendicular to the interface with the trivial background state. Figure 9 indicates that such structures indeed exist but that they do not snake. Nonsnaking of these structures is consistent with their spatial-dynamics interpretation. As indicated in Figure 9, roll patterns that are comprised of rolls that are oriented parallel to the y-direction are periodic in x but constant in y and correspond therefore to equilibria of the y-dynamical system. Thus, the corresponding localized rolls can be interpreted as homoclinic orbits in the y-evolution that bifurcate from a heteroclinic cycle that involves only equilibria, namely the trivial state $U = 0$ and the parallel roll pattern. In particular, the discussion in section 2 implies that snaking should not occur. Direct numerical simulations indicate that the localized rolls in Figure 9 are again alternately stable and unstable between saddle-node bifurcations.

4.2. Almost planar localized rolls. The spatial-dynamics interpretation of the localized roll patterns discussed in Figures 8 and 9 allowed us to predict quite easily whether they should snake or not. In this section, we consider localized patterns that can exhibit both snaking and nonsnaking behavior depending on the parameter direction in which we continue them. In particular, the initial shape of the pattern is not sufficient to predict snaking or nonsnaking.

Our starting point is the pattern shown in panel 1 of Figure 10, which was found in [9] via direct numerical simulations for $\nu = 2$. We use algorithm 1 to continue this pattern in the parameter μ and refer to the accompanying movie file (78274_01.mpg [2.4MB]) for a complementary visualization of the patterns we found. Upon continuing initially in the direction of decreasing μ, we observe the nonsnaking scenario. As shown in panel 2 of Figure 10 and in more detail in Figure 11, vertical rolls are formed at both ends of the pattern that

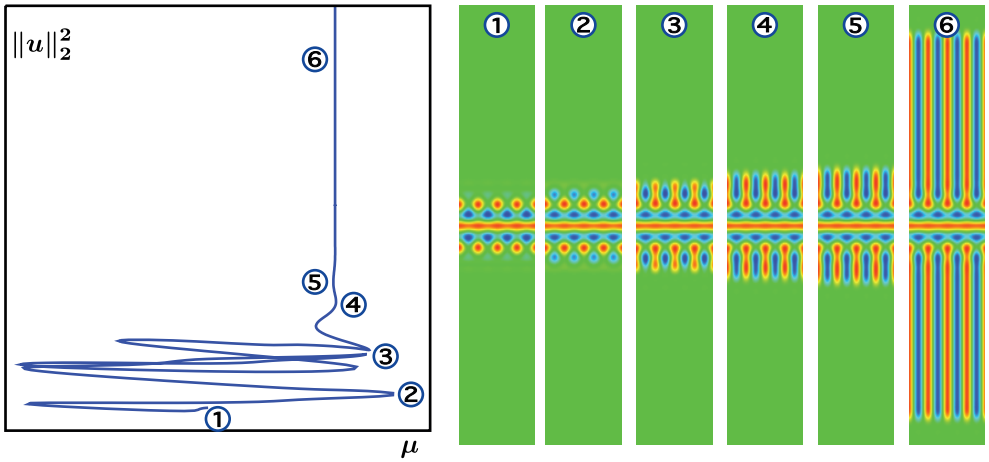

Figure 11. *The nonsnaking branch of the bifurcation diagram from panel 2 in Figure 10 is displayed in more detail. As we move along the branch, the solution develops blue and red spots along the interface. These red spots subsequently develop into vertical stripes, which progressively cover the entire domain. The vertical asymptote occurs at the Maxwell point* $\mu_r = 0.6753$ *of the 1D rolls.*

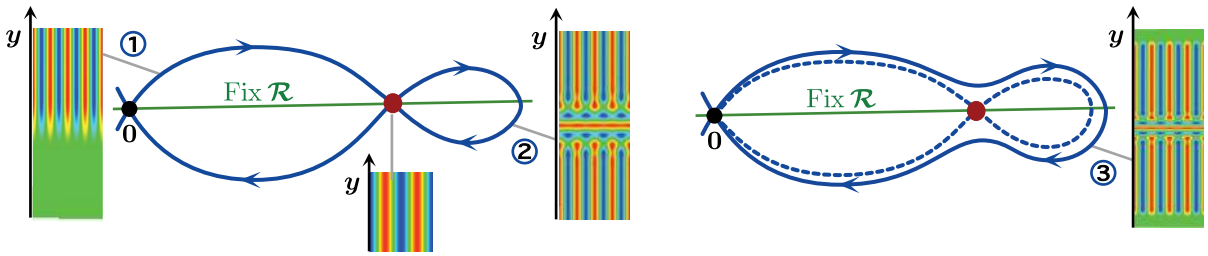

Figure 12. *We illustrate the spatial-dynamics interpretation of the y-dynamics of almost planar stripes along the nonsnaking branch. We can interpret the almost planar stripe pattern shown in the right panel as a homoclinic orbit to* $U = 0$ *that bifurcates from the heteroclinic network shown in the left panel. The heteroclinic network consists of a codimension-one heteroclinic cycle between* $U = 0$ *and vertical 1D rolls, which exists only at the Maxwell point of 1D rolls, and a robust reversible homoclinic orbit to vertical 1D rolls. Note that vertical 1D rolls are equilibria in the y-dynamics.*

then grow in length as we move along the branch. The bifurcation branch itself approaches the vertical asymptote $\mu_r = 0.6753$, which corresponds to the Maxwell point of 1D rolls. As indicated in Figure 12, this behavior can be explained as follows by spatial dynamics in the y-variable. An almost planar stripe pattern corresponds to a reversible homoclinic orbit that connects the trivial state to itself but that also stays for long times y near the equilibrium that corresponds to the vertical 1D roll structure. It is then natural to postulate the existence of a heteroclinic network in the y-dynamics that consists of a heteroclinic cycle that connects $U = 0$ to the equilibrium corresponding to vertical 1D rolls and a homoclinic orbit that connects the latter equilibrium to itself. The homoclinic orbit is $\mathcal{R}$-reversible and therefore robust. The heteroclinic orbits forming the heteroclinic cycle, on the other hand, will have codimension one, as they can exist only at the Maxwell point. Since the heteroclinic network involves only equilibria and no periodic orbits when interpreted in terms of the y-dynamical

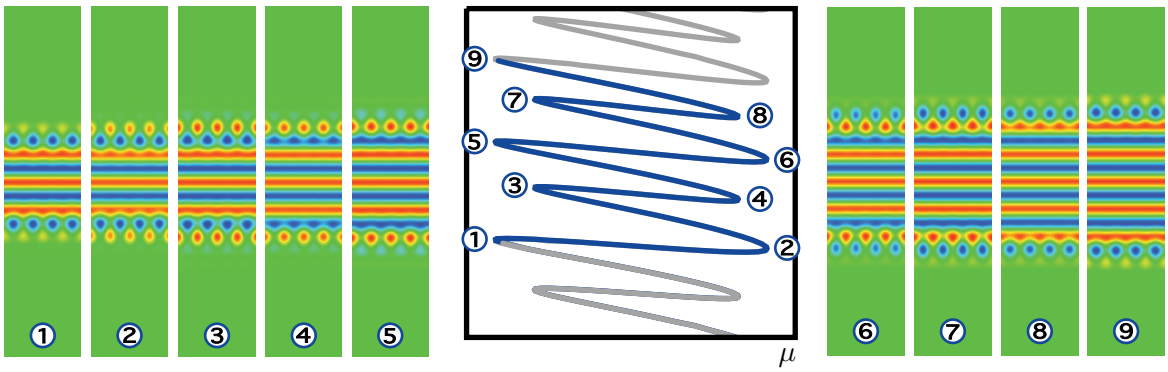

Figure 13. *In the center, we show a section of the snaking branch from panel* 3 *of Figure* 10*. As we move along the branch, the pattern grows horizontal stripes via a sequence of nine saddle nodes, as shown in panels* 1–9*. For the pattern shown in panel* 1*, the interface between rolls and the trivial state is made up of blue spots. As we move up on the branch through panels* 2–5*, red spots are added to the interface, while the blue spots merge to form the first half of a new roll. Panels* 6–9 *show the development of new blue spots along the interface, while the red spots merge to complete the formation of the new roll seen in panel* 9*. Inspecting panels* 1 and 5*, we find that the interface regions, plotted here over four full periods in* x *so that* $x \in (0, 8L_x)$*, are related by the symmetry operator* κ*, which corresponds to multiplication of the pattern by* -1 *and reflecting it in* x *across* $x = L_x$*.*

system, we are in the nonsnaking case.

We now return to Figure 10 and discuss panel 3, which we obtained when we continued the almost planar stripe pattern from panel 1 initially in the direction of increasing μ. The spatial-dynamics interpretation of the pattern shown in panel 3 of Figure 10 is the same as that shown in Figure 8 for a planar stripe pattern, which explains the snaking behavior visible in Figure 10. Interestingly, the saddle nodes along the snaking branch are aligned along four vertical asymptotes instead of the usual two vertical limits. The details of the profile changes that occur at these saddle-node bifurcations are shown and explained in Figure 13. Note that all patterns are reversible under the reverser $\mathcal{R}$ that acts through $y \mapsto -y$. Moving up from one saddle node to the next, say from panel 1 to panel 5 in Figure 13, we see that the interface regions of the two patterns are related by the symmetry operator κ that acts through $u(x, y) \mapsto -u(L_x - x, y)$. Thus, from the results in [5] that we discussed in section 2, we expect the complete bifurcation diagram to be as shown in Figure 6. In particular, there should be a second distinct branch of patterns with $\kappa\mathcal{R}$-symmetry, whose bifurcation curve is shifted vertically in the $\|u\|_{L^2}^2$-direction by half of the curve's vertical period. Furthermore, various ladder branches corresponding to asymmetric patterns should exist. Before discussing these structures in detail, we mention that our spectral computations indicate that the patterns from Figure 13 are alternately stable and unstable with respect to perturbations on $\Omega_{\frac{1}{2}}$ with Neumann boundary conditions; see Figure 14. Thus, the sketch given in Figure 6 correctly reflects the stability properties along the primary snaking curve of $\mathcal{R}$-symmetric patterns.

Our goal is now to verify, via numerical computations, that the overall bifurcation structure of the almost planar stripe patterns, including their stability properties, is exactly as predicted in Figure 6. As already mentioned, the almost planar stripe patterns presented in Figure 13 are $\mathcal{R}$-symmetric, so that $u(x, y) = u(x, -y)$ for all (x, y). The patterns with $\kappa\mathcal{R}$-symmetry,

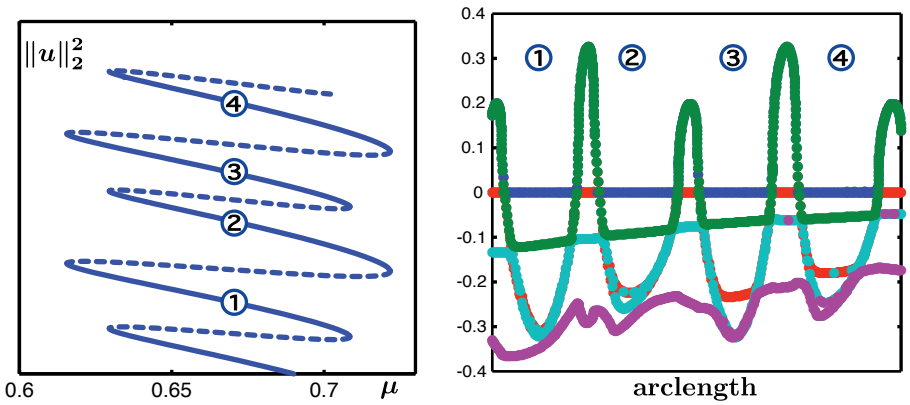

Figure 14. *The stability of the $\mathcal{R}$-symmetric almost planar stripes from Figure 13 with respect to even perturbations is indicated in the left panel by solid (stable) and dashed (unstable) lines. On the unstable branches, there are two unstable eigenvalues: one unstable eigenvalue is associated with the saddle-node bifurcation, while the other one is due to a pitchfork instability that breaks the $\mathcal{R}$-symmetry. The right panel shows the eigenvalues of the linearized problem plotted along the branch. Computations are done using algorithm 3 with $n_x = 8$, $n_y = 800$, and $L_y = 50$.*

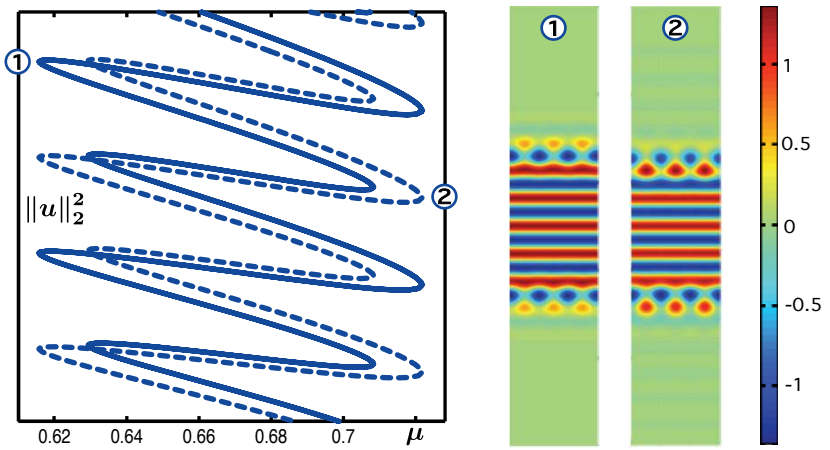

Figure 15. *The solid branch corresponds to almost planar stripe patterns with $\mathcal{R}$-symmetry, while the dashed branch corresponds to solutions with $\kappa\mathcal{R}$-symmetry. The saddle-node limits are $\mu = 0.6157$, $0.6293, 0.7084, 0.7218$, and the Maxwell point of 1D rolls occurs at $\mu_r = 0.6753$. This branch is computed using algorithm 2 with $L_y = 100$ and* NTST$= 200$.

whose existence we conjectured above, would satisfy $u(x, y) = -u(L_x - x, -y)$ for all (x, y); that is, they should not change when simultaneously reflecting in y, reflecting in x across the midperiod point, and multiplying the pattern by -1. In Figure 15, we present numerical computations of these anticipated $\kappa\mathcal{R}$-symmetric almost planar stripe patterns that exist along a snaking branch that is shifted vertically as conjectured.

Next, we computed the ladder branches of asymmetric structures that are predicted by the analysis in [5] and sketched in Figure 6. The asymmetric patterns bifurcate via pitchfork bifurcations from the symmetric patterns. These pitchforks occur exponentially close in L

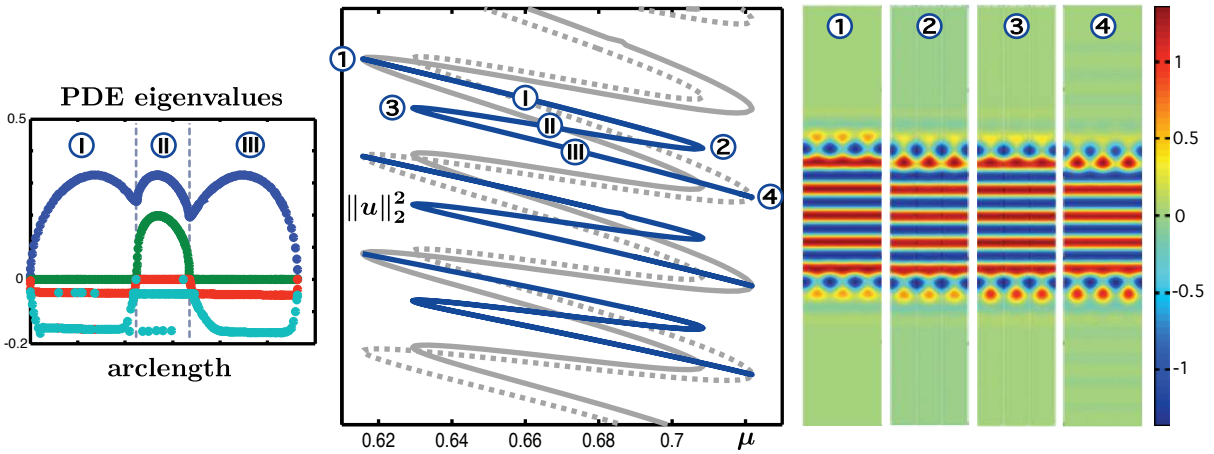

Figure 16. *Shown are the cross-connecting ladder branches of asymmetric patterns that connect the branch of $\mathcal{R}$-symmetric patterns from Figure 15 to the branch of $\kappa\mathcal{R}$-symmetric patterns. The four rightmost PDE eigenvalues of the asymmetric states along the ladder branches are shown in the left panel: all solutions are unstable. All ladder branches are computed with algorithm 3 using $n_x = 4$, $n_y = 800$, and $L_y = 50$.*

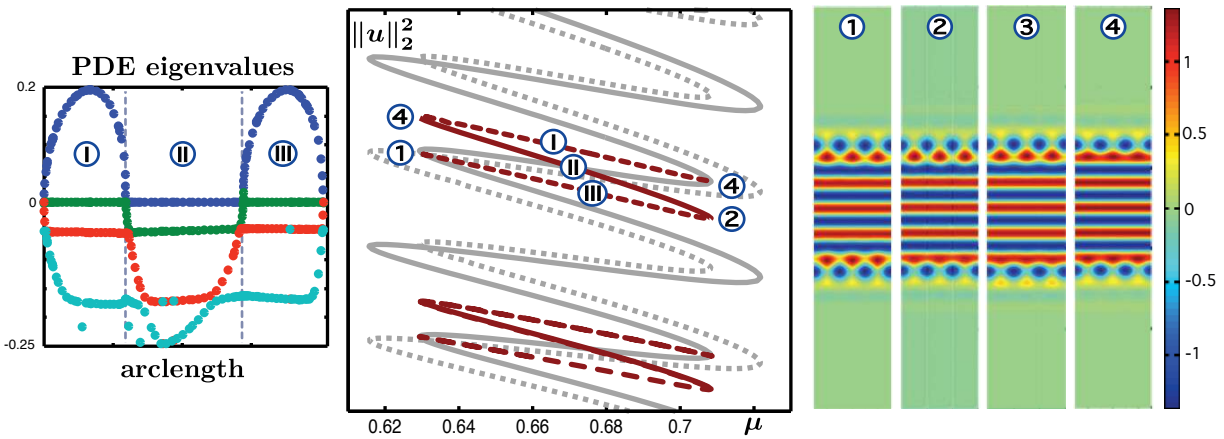

Figure 17. *Shown are the reconnecting ladder branches of asymmetric patterns that begin and end at the branch of $\mathcal{R}$-symmetric patterns from Figure 15. The four rightmost PDE eigenvalues of the asymmetric states along a ladder branch are shown in the left panel, indicating that these patterns are stable along the middle parts of each ladder branch. The computational details are as in Figure 16.*

to the fold bifurcation. Furthermore, the results in [5] show that the ladder branches that emerge near the inner folds connect back to the same branch of symmetric patterns, while the ladder branches that emanate from the outermost folds along the branch of $\mathcal{R}$-symmetric structures connect to the branch of $\kappa\mathcal{R}$-symmetric structures, and vice versa; we shall refer to the former branches as reconnecting and to the latter branches as cross-connecting. The numerical continuation results shown in Figures 16 and 17 confirm these findings. We also computed the rightmost eigenvalues of the PDE linearization about the asymmetric stripe patterns and found that these patterns are unstable along the cross-connecting branches and stable along the middle parts of the reconnecting branches. To test the analytical prediction for

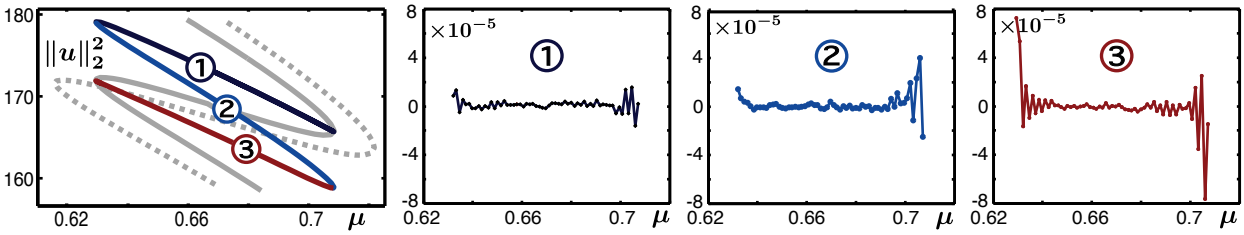

Figure 18. *We compare the numerically computed ladder branches and the curves predicted from the snaking branch using the equation $z(L+\varphi) = z(L-\varphi)$. The larger errors at the end points of the ladder branches are due to interpolation errors that arise since we used an equidistant interpolation mesh which leads to the Runge phenomenon. The interpolation is done with 60 points along each branch.*

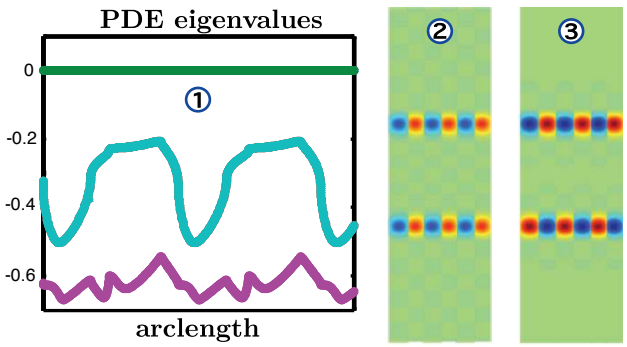

Figure 19. *The four rightmost Dirichlet eigenvalues of the patterns shown in Figure 13 are plotted in panel 1 against the arclength along the branch. Two of these eigenvalues are very close to zero, and the resulting eigenfunctions are shown in panels 2 and 3. One of the small eigenvalues sits at zero and is enforced by the translation symmetry in the periodic x-direction, while the other one reflects the fact that the almost planar stripe patterns can be thought of as bound states (see main text for details). Computations were performed with algorithm 3 using $n_x = 4$, $n_y = 800$, and $L_y = 50$.*

the asymmetric states, we plot in Figure 18 the difference between the numerically computed solution branches and the curves computed from the symmetric branch via the equation $z(L+\varphi) = z(L-\varphi)$, for which we find excellent agreement.

The spectral computations presented so far address linear stability with respect to perturbations that satisfy Neumann boundary conditions at $x = 0$ and $x = L_x$ (and therefore on the boundary of the computational domain $\Omega_{\frac{1}{2}}$; see Figure 7). To address spectral stability on the full cylindrical domain Ω_1 with periodic boundary conditions in x, it suffices to compute the spectrum on $\Omega_{\frac{1}{2}}$ with Dirichlet boundary conditions at $x = 0$ and $x = L_x$. In Figure 19, we plot the Dirichlet spectrum of the almost planar stripe patterns given in Figure 13, but note that we obtained similar results for the other symmetric and asymmetric patterns that we computed above. Figure 19 shows that these patterns have two Dirichlet eigenvalues near zero. One of these eigenvalues arises due to the translational symmetry in x and should therefore sit exactly at the origin. The other eigenvalue arises due to the bound-state nature of our solutions. Indeed, the central part of each almost planar stripe pattern consists of horizontal roll patterns that are approximately constant in the x-direction. Thus, if we shift the solution

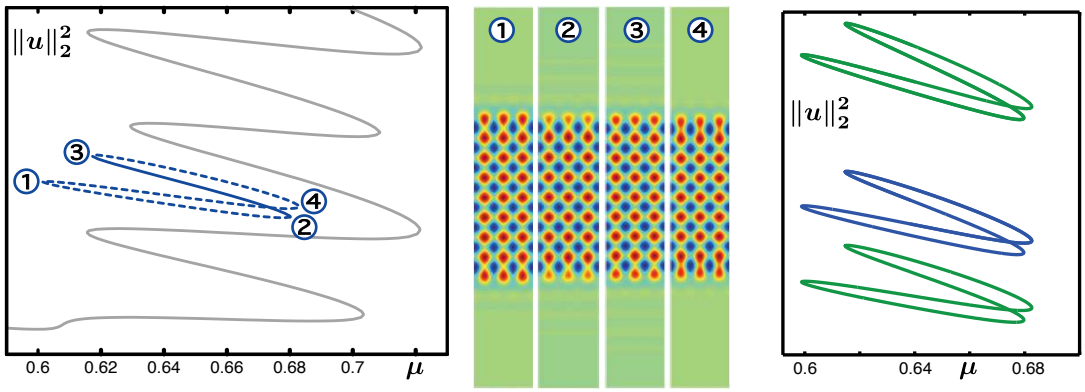

Figure 20. *The left and right panels contain isolas of localized square patterns for $\nu = 2$. In the left panel, stable and unstable solutions along the isola are indicated by solid and dashed curves, respectively; the isola from the left panel is drawn in blue in the right panel. Algorithm 2 was used with $y \in [0, 200]$ and* NTST $= 400$.

in the upper and lower halves of the domain against each other in the x-direction, the resulting pattern is still an approximate solution. Among this one-parameter family of approximate patterns, which is parametrized by the relative shift in the x-direction, there are two exact solutions, one of which is $\mathcal{R}$-symmetric, while the other has $\tau\mathcal{R}$-symmetry. We expect that one of these two symmetric patterns is stable under periodic boundary conditions, while the other one is unstable in the direction of the shift x.

4.3. From localized stripe to square patterns. For the almost planar stripe patterns that we discussed in the previous section, we observed the growth of square cells along the interface between rolls and the trivial state that then merged to form new rolls. This observation led us to examine localized square patterns on the cylinder. Figure 20 contains continuation results for localized square patterns that we found near the Maxwell point $\mu_s = 0.609$ of domain-filling square patterns. The pattern profiles from panels 1–4 show that new squares are grown at the interface with the trivial state. The bifurcation curve is an isola, though, and snaking does not occur. It appears as if the snaking of the pattern is inhibited by the relative proximity of the roll structures: panel 4 indicates that the localized square pattern tries to grow vertically oriented rolls. Note that the localized square patterns shown in Figure 20 seem to be stable along part of the bifurcation curve, which indicates that domain-covering square patterns are stable in this parameter region. This is surprising since domain-covering square patterns are known to be unstable at onset in the cubic-quintic Swift–Hohenberg equation [14].

To further explore the interaction between stripe and square patterns, we lowered the value of ν to 1.06247 and again continued localized almost planar stripe patterns in μ. The results, shown in Figure 21, indicate that the bifurcation structure is qualitatively similar to that shown in Figure 10 for $\nu = 2$. Starting from the pattern shown in panel 1 of Figure 21, one side of the branch approaches a vertical asymptote given by the Maxwell point of 1D rolls, while the other side of the branch snakes. Along the nonsnaking branch, the pattern grows four rows of squares, as in panels 2–5, before eventually growing vertically oriented rolls, as in panel I. Along the snaking branch, an interior plateau of horizontally oriented rolls develops, as shown in panel II. There are a few interesting differences, both in terms of the shape of

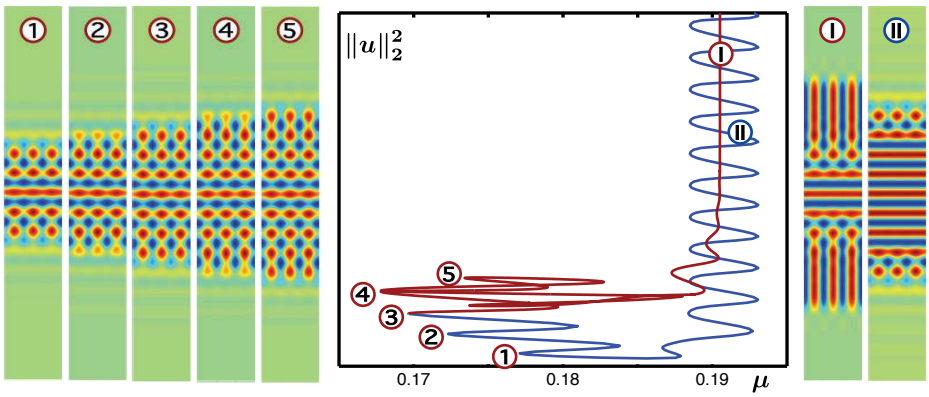

Figure 21. *The bifurcation diagram of almost planar stripe patterns is shown for* $\nu = 1.06247$. *The Maxwell points of rolls and squares occur at* $\mu_r = 0.1905$ *and* $\mu_s = 0.1716$, *respectively. The branch is computed with algorithm* 2 *with* $y \in [0, 200]$ *and* NTST $= 300$.

the profiles and the details of the bifurcation curves, when comparing Figures 10 and 21. In the latter figure, many more rows of squares are grown, indicating that the Maxwell points of squares and rolls are much closer to each other so that these patterns can bind more strongly to each other. Second, there are only two saddle-node asymptotes along the snaking branch shown in Figure 21 compared with four limits in Figure 10. In particular, for $\nu = 1.06247$, we expect to find only horizontal ladder states of asymmetric localized stripe patterns similar to those shown in Figure 1, compared with the more complicated bifurcation structures visible in Figures 16 and 17 for $\nu = 2$.

To determine which of the two left and two right folds for $\nu = 2$ collide and disappear when we decrease ν, we continued these folds in two parameters. Figure 22 contains the resulting two-parameter bifurcation diagram with the four fold curves of the almost planar stripe patterns from Figure 13 and the Maxwell curves associated with stripes and squares. We find that the leftmost and right-interior folds of the stripe patterns shown in Figure 13 collide in a cusp bifurcation at $(\mu, \nu) = (0.401, 1.57)$, while the rightmost and left-interior folds from Figure 13 disappear in a cusp at $\nu = 0.758$. These results explain why the snaking curve in Figure 22 for $\nu = 1.06247$ involves only two vertical asymptotes. To illustrate these results further, we plot in Figure 23 the bifurcation curves of almost planar stripe patterns for various values of ν, while tracking the location of all folds along the snaking diagram. We see again how the leftmost fold collides with the innermost right fold for $\nu \approx 1.57$. Note that different ladder branches for asymmetric patterns will collide and reorganize themselves near the parameter values corresponding to the first, third, and fifth panels in Figure 23, where the folds change their relative position in the μ-direction: the theory developed in [5] can be used quite straightforwardly to analyze the resulting global bifurcations, but we shall not present these details here.

Note that the Maxwell curves for stripes and squares shown in Figure 22 both emerge from the codimension-two point $(\mu, \nu) = 0$. The proximity of the Maxwell curves for squares and rolls suggests that snaking in the cubic-quintic Swift–Hohenberg equation may be very intricate. Indeed, the numerical computations in [8, 9] indicate that the snaking behavior of

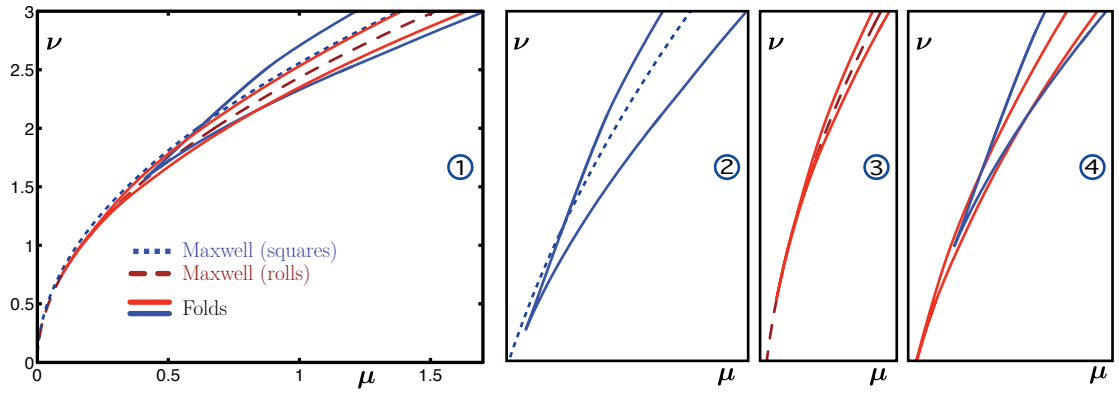

Figure 22. *The left panel shows four saddle-node bifurcation curves of the almost planar localized stripe patterns from Figure 13 in the (μ,ν)-plane, together with the Maxwell curves associated with domain-filling roll and square patterns. The leftmost and right-interior folds in Figure 13 are plotted in red, while the rightmost and left-interior folds in Figure 13 are shown in blue. The remaining three panels contain enlarged portions of panel 1.*

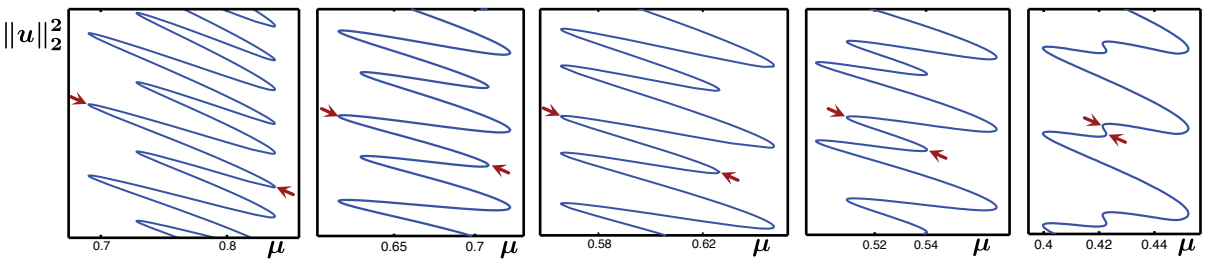

Figure 23. *The bifurcation diagrams of almost planar stripe patterns are shown for $\nu = 2.153$, 2, 1.895, 1.806, 1.599 from left to right. The arrows indicate which of the folds correspond to each other upon varying ν.*

localized patterns in one dimension is very complicated in the presence of multiple Maxwell points.

5. Fully localized planar stripe patterns. In this section, we investigate the parameter dependence of fully localized planar stripe patterns, which we refer to as *worms* by analogy with similar but time-dependent structures first observed in electroconvection in nematic liquid crystals [25, 18]. In the planar Swift–Hohenberg equation, time-independent states of this type were first found in [37] using direct numerical simulation. In both systems, these states are located in the subcritical regime [37, 6]. Our goal is to investigate via continuation methods whether worm structures in the Swift–Hohenberg equation snake or not. We found stationary worms initially by continuing radial spots from which worms bifurcate in symmetry-breaking bifurcations. This is similar to the case of fully localized planar hexagon patterns that were discussed in [31] for the quadratic-cubic Swift–Hohenberg equation: the hexagon patches also bifurcated from radial spots and were found to snake in a complicated fashion that is not yet fully understood. All computations in this section are carried out using algorithm 1 for large values of L_x.

Figure 24 contains two disjoint branches of fully localized stripe patterns for $\nu = 2.50081$.

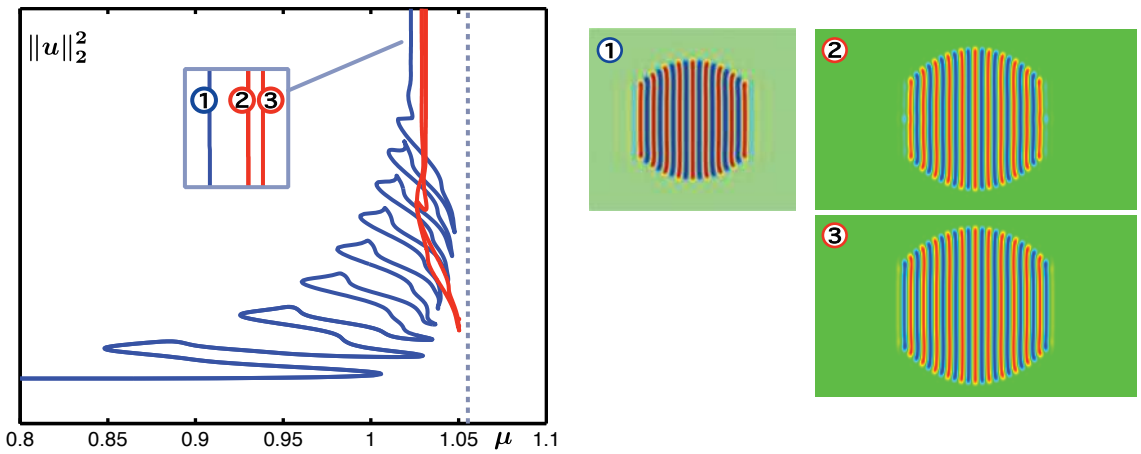

Figure 24. *The left panel contains two disjoint branches of fully localized planar stripe patterns and the Maxwell point* $\mu_r = 1.0560$ *of* 1*D rolls shown as the vertical dashed line. The blue curve, which corresponds to the worm patches with* 9 *rolls shown in panel* 1*, approaches the vertical asymptote* $\mu = 1.0228$*. For comparison, the Maxwell point of* 1*D localized roll patterns comprised of* 9 *rolls is given by* $\mu = 1.0023$*. The red curve corresponds to the worm patches with* 11 *rolls shown in panels* 2–3*: its limiting vertical asymptotes are* $\mu = 1.0290$ *and* $\mu = 1.0314$*. The Maxwell points of localized* 1*D roll patterns with* 11 *rolls are* $\mu = 1.0285$ *and* $\mu = 1.0313$*. The red curve has been rescaled linearly in the vertical direction to fit into the same graph. The computations were done for* $\nu = 2.50081$ *with* $L_x = 90$*,* $L_y = 90.38$*, and* $n_x = n_y = 220$*.*

The branch shown in blue emanates from a branch of radial spots and begins to snake, but eventually ceases to snake and instead approaches a single vertical asymptote. During the snaking phase, the worm profiles acquire an additional pair of vertically aligned rolls at each fold bifurcation, thus making the patterns shown in panel 1 of Figure 24 wider in the horizontal x-direction as we move up along the branch. As snaking ceases and the branch approaches its vertical asymptote, the number of rolls, and therefore the horizontal width, of the localized worm pattern stays constant; instead, the rolls grow along the vertical y-direction, thus making the pattern more elongated in the vertical direction, which leads to the observed increase of its L^2-norm. Figure 24 contains a second branch, shown in red, which starts and ends at infinite L^2-norm and can therefore be thought of as an isola of localized worm patterns. The worm profiles consist of 11 rolls whose vertical length changes along the branch to generate the change in L^2-norm visible in Figure 24. As shown in the inset, this second branch exhibits two different vertical asymptotes.

Surprisingly, the three asymptotes of the branches plotted in Figure 24 are relatively far away from the Maxwell point of domain-filling 1D rolls, and we now put forward an explanation of this discrepancy using spatial-dynamics arguments. Figure 25 contains spatial-dynamics interpretations of the initial snaking period and the eventual nonsnaking regime in the left and right panels, respectively, that are similar to those for the almost planar stripe patterns that we discussed in the previous section. The key difference between worms and planar stripe patterns is that the heteroclinic cycles for the y-dynamical system that describe worms do not involve domain-filling 1D rolls as in the case of planar stripe patterns. Instead, the limiting equilibria are localized 1D rolls $u_n(x)$ that consist of a finite number of 1D rolls, given by the

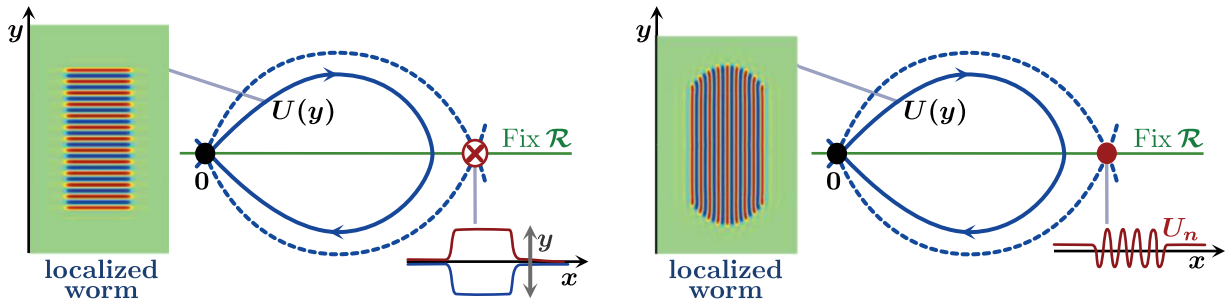

Figure 25. *The left panel shows a fully localized stripe pattern with rolls that are aligned horizontally. If only the vertical length of this pattern (and therefore its L^2-norm) increases during continuation, while its horizontal width stays constant, then the stripe patches can be interpreted as homoclinic orbits of the y-dynamical system, which bifurcate from a heteroclinic cycle between the equilibrium $U = 0$ (indicated by a solid circle) and the y-periodic orbit (indicated by a circled cross) that corresponds to the horizontally aligned rolls that are localized in the x-direction. This scenario is expected to lead to snaking. The right panel shows a worm patch that consists of n vertical rolls. If the number of rolls stays constant during continuation, and the patterns grow only in the vertical y-direction, then we can interpret these patterns as homoclinic orbits for the y-dynamics that connect the trivial state to itself and stay for long times near the equilibrium that consists of a localized 1D roll pattern $U_n(x)$ comprised of n rolls. These homoclinic orbits may arise from a heteroclinic cycle that connects the equilibria $U = 0$ and $U = U_n$: this cycle has codimension one, and we expect to encounter the nonsnaking case.*

number n of vertical rolls that make up the localized worm patch. These heteroclinic cycles should exist only at the Maxwell point of the localized 1D roll patterns $u_n(x)$, where $\mathcal{H}(u_n)$ vanishes. In the caption of Figure 24, we compare the Maxwell points of the 1D pulses that consist of 9 and 11 rolls with the asymptotes of worm patches with 9 and 11 rolls and find excellent agreement. Figure 26 contains a more detailed comparison of the worm with 11 rolls and the associated 1D pulse. We remark that there are two 1D pulses with vanishing Hamiltonian $\mathcal{H}$ for each given number of rolls. These two pulses lie on the same snaking branch but are separated by a single fold bifurcation. Thus, one of them is stable, while the other is unstable. Inspecting the red branch in Figure 24 that corresponds to worms with 11 rolls and noting that this branch exhibits two different asymptotes given by the two 1D pulses with vanishing Hamiltonian that have 11 rolls, we therefore expect that worms are stable along one part of the branch and unstable along the other part: Figure 27 contains a comparison of the rightmost PDE eigenvalues of 1D pulses and worms with 11 rolls along their respective branches that confirms this expectation.

The results presented so far indicate that branches of fully localized stripe patterns with n interior rolls should approach vertical asymptotes given by 1D pulses with vanishing Hamiltonian that consist of n rolls. In the right panel of Figure 28, we plot the branches of 1D pulses with vanishing Hamiltonian in the (μ, ν)-plane for values of n between 2 and 11 rolls. As we decrease ν, the two branches corresponding to the stable and unstable 1D pulses with n interior rolls disappear in fold bifurcations: the branches for different values of n disappear in the ordering given by n, with branches for smaller n vanishing first. This indicates that we should be able to find worms with a small number of interior rolls only for large values of ν. Figures 29 and 30 contain continuation results of worms for $\nu = 3$ and $\nu = 2$, respectively, that start from radial spots. While the worms in Figure 29 contain only a few rolls, the patterns

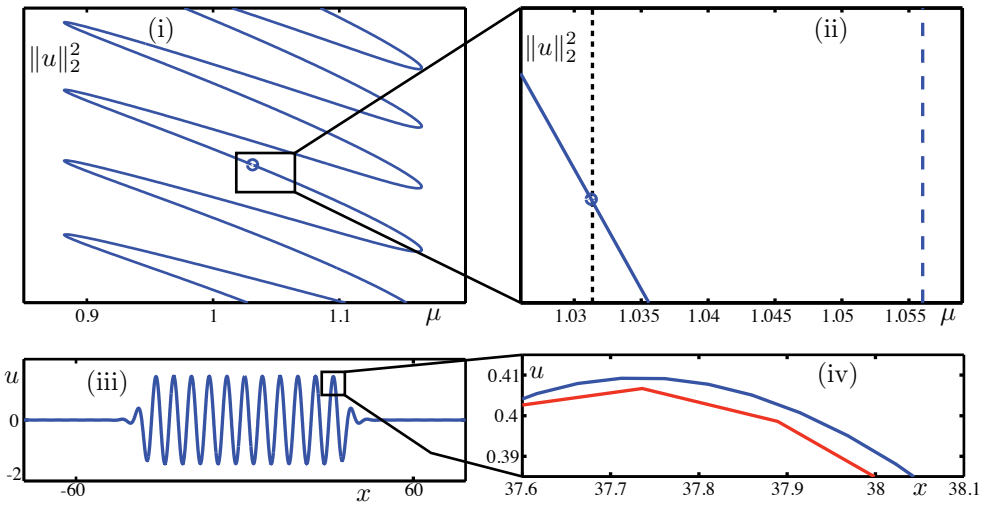

Figure 26. *Panel* (i) *shows the bifurcation diagram of localized* 1*D rolls at* $\nu = 2.50081$. *The blue circle at* $\mu = 1.0313$ *denotes the location of the* 1*D pulse with* $\mathcal{E} = 0$ *that consists of* 11 *rolls: its profile is shown in panel* (iii). *Panel* (ii) *shows a segment of the bifurcation curve near this* 1*D pulse together with the Maxwell point* $\mu = 1.0560$ *of* 1*D rolls, shown as a vertical dashed line, and the vertical asymptote* $\mu = 1.0314$ *of the fully localized worm patch comprised of* 11 *rolls from panel* 3 *in Figure* 24, *as a vertical dotted line. In panel* (iv), *we compare the pulse profile (in blue) and the transverse worm profile along the* x*-direction for fixed* y *(in red).*

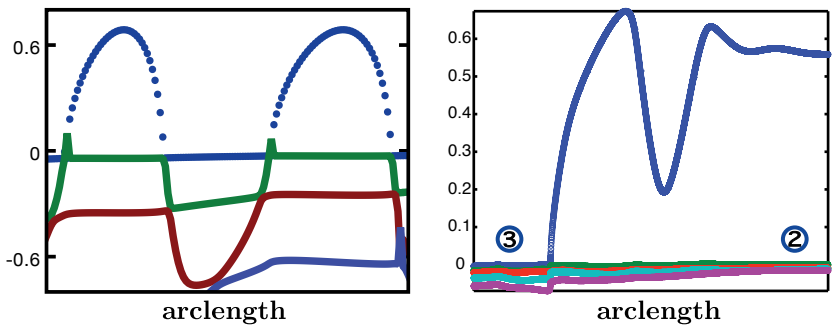

Figure 27. *The left and right panels show, respectively, the rightmost PDE eigenvalues along the snaking curve of localized rolls from Figure* 26 *and along the red branch of fully localized planar stripe patterns with labels* (2) *and* (3) *from Figure* 24 *at* $\nu = 2.50081$. *The eigenvalues are parametrized by arclength along the underlying solution branches.*

shown in Figure 30 have a large number of interior rolls, as predicted by Figure 28.

It is natural to ask how the branches of fully localized stripe patterns acquire additional fold bifurcations as we decrease ν or, in other words, how the branches shown in Figures 29 and 30 transform into each other upon decreasing ν. It turns out that the mechanism is quite complicated and, interestingly, involves isolated branches such as the rightmost branch from Figure 24. To illustrate the creation of new folds, we present in Figure 31 continuation results for two nearby values of ν. We see that the snaking branch and a second isolated branch collide and rearrange themselves, leading to an additional fold bifurcation and therefore an

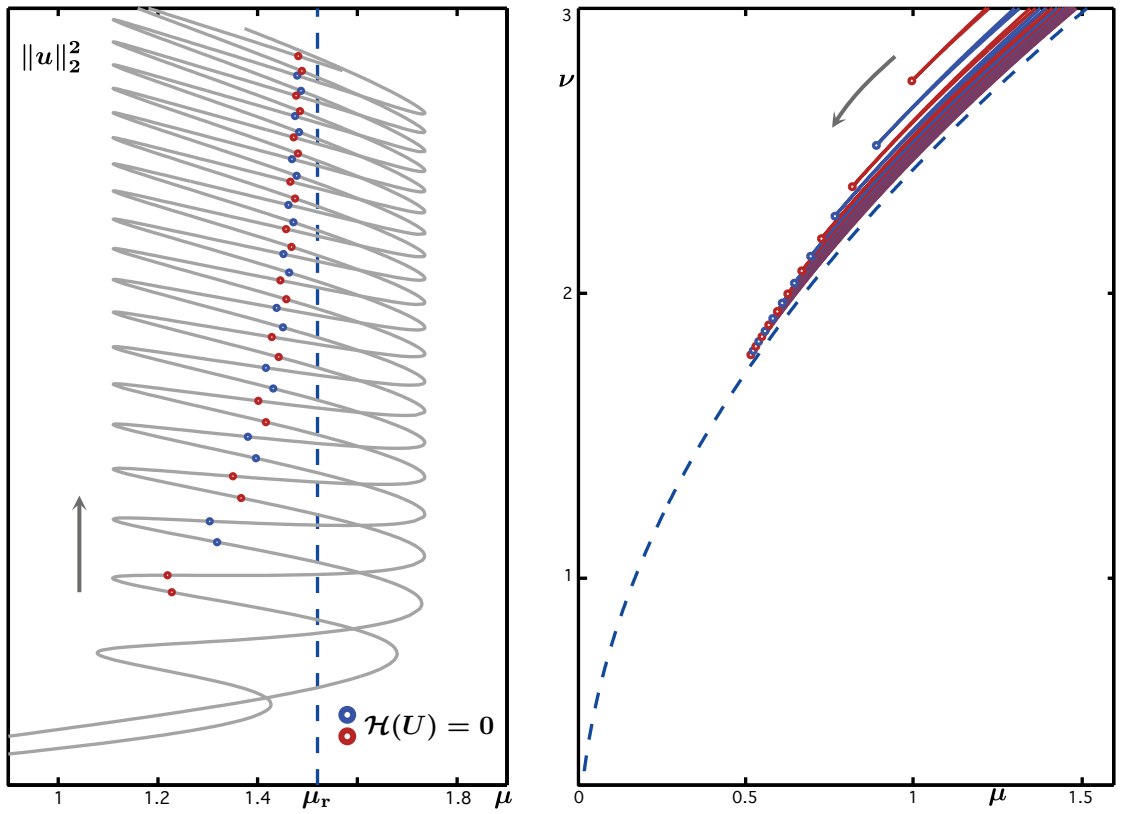

Figure 28. *The left panel contains the two snaking branches of localized* 1*D pulses for* $\nu = 3$*. Pulses with vanishing Hamiltonian* $\mathcal{H}$ *are labelled with circles, and we see that the corresponding values of* μ *tend to the Maxwell point of* 1*D rolls, indicated by the vertical dashed line, as the pulse width tends to infinity. The two lowest red circles correspond to pulses with* 2 *rolls, while the pulses at the two topmost red circles consist of* 11 *rolls; two rolls are added at each left fold bifurcation. Continuing* 1*D pulses with vanishing Hamiltonian for different pulse widths in the* (μ, ν)*-plane leads to the diagram shown in the right panel, where the dashed curve is the Maxwell curve of* 1*D rolls.*

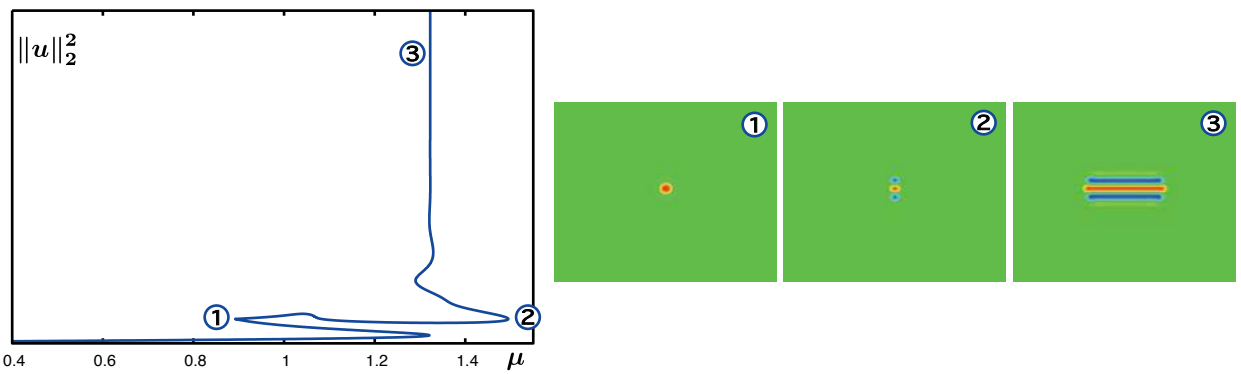

Figure 29. *A branch of fully localized planar stripe patterns that consist of one roll is shown in the left panel for* $\nu = 3$*. As we move up on the branch towards label* (3)*, the horizontal width of the stripe pattern increases. The computations were done with* $L_x = 90$*,* $L_y = 90.38$*, and* $n_x = n_y = 220$*.*

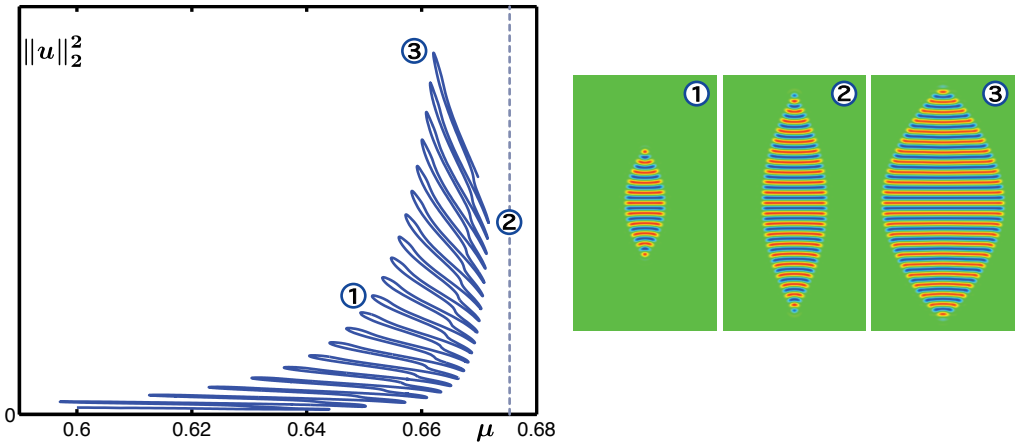

Figure 30. *A branch of fully localized planar stripe patterns at $\nu = 2$ is shown in the left panel. The Maxwell point of 1D rolls that occurs at $\mu = 0.6753$ is shown as a vertical dashed line. The computations were done with $L_x = 43.9823$, $L_y = 78.5398$, $n_x = 129$, and $n_y = 513$.*

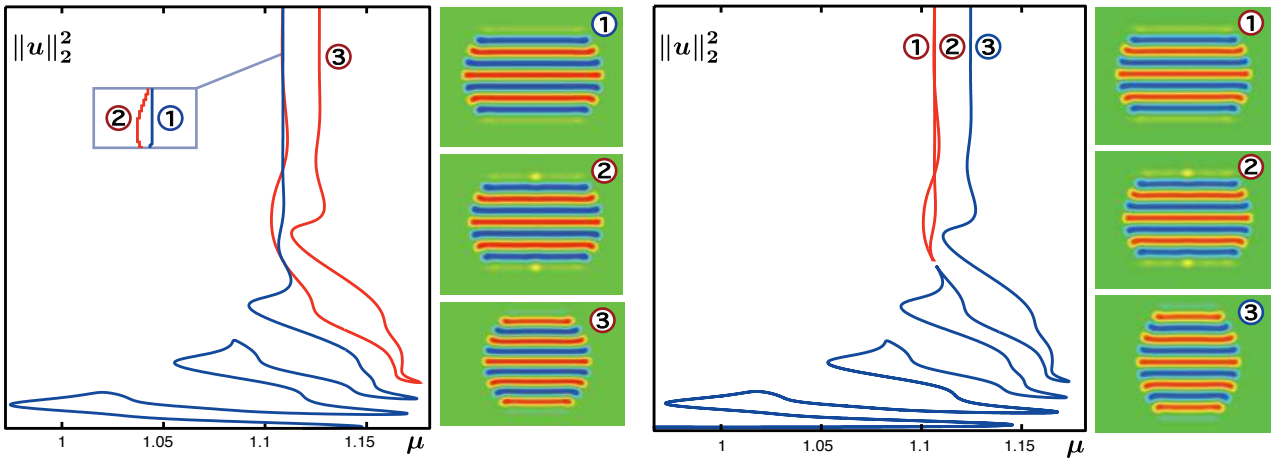

Figure 31. *Two branches of fully localized stripe patterns are shown for $\nu = 2.655$ (left) and $\nu = 2.652$ (right). The blue snaking branch and the leftmost branch of the red isola in the left panel collide and rearrange themselves upon decreasing ν, leading to the red isola and the blue snaking branch shown in the right panel. As a result, the emerging blue branch in the right panel snakes for longer. The numerical parameters are $L_x = L_y = 90$ and $n_x = n_y = 220$.*

increase of the number of rolls inside the fully localized structures along the snaking branch. When ν is decreased further, the rightmost blue branch in the right panel of Figure 31 moves towards the left and eventually collides again with the leftmost red branch, leading to a rearrangement similar to that shown in Figure 31. As indicated in Figure 32, this mechanism of adding additional folds along the branch seems to continue indefinitely upon decreasing ν further. We remark that the constant changes of the relative position of the different branches under variations of ν make it difficult to compute them using direct continuation in ν. Instead, we continued fold bifurcation curves in the parameters (μ, ν) and afterwards

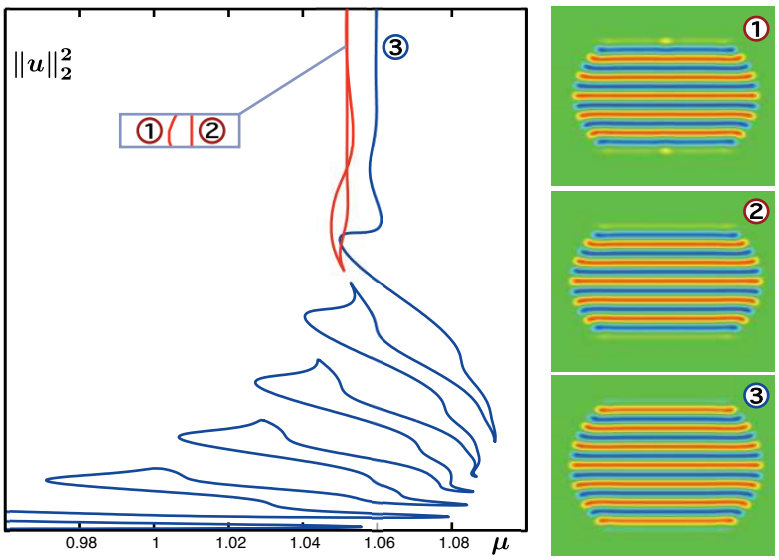

Figure 32. *The two branches of fully localized stripe patterns from Figure 31 are shown for $\nu = 2.556$. The bifurcation structure shown here indicates that the process of collision and subsequent rearrangement of branches that we observed in Figure 31 repeats itself upon decreasing ν further, thus leading to more extended snaking curves such as the one plotted here. The numerical parameters are $L_x = L_y = 90$ and $n_x = n_y = 220$.*

restarted continuation in μ from these folds for different fixed values of ν.

The pattern shown in Figure 30 for $\nu = 2$ looks quite different from the worm patches shown in the other figures for larger values of ν: the top and bottom caps of the patterns for $\nu = 2$ are peaked instead of flat. Figure 33 and the accompanying movie file (78274_02.mpg [3.9MB]) illustrate this spatial behavior further. In particular, the sign of the curvature near the peaked top and bottom ends of the worm patches seems to change along the snaking branch. This phenomenon is not explained by our spatial-dynamics interpretation, and we discuss it further in section 6.

6. Discussion.

In this paper, we presented a comprehensive numerical study of localized stripe patterns for the planar cubic-quintic Swift–Hohenberg equation. The main motivation was our desire to connect the profiles of planar patterns and the shape of their bifurcation branches to relatively simple ideas from dynamical systems theory. We hope that we convinced the reader that these ideas can explain snaking and nonsnaking of solution branches and elucidate the mechanisms that lead to changes of the profiles along these branches. We have also seen, however, that there are many questions that cannot, at this stage, be addressed using spatial dynamics, and in the remainder of this section we outline some of the remaining issues together with other open problems.

Spatial dynamics is most predictive when there is one distinguished direction in which patterns grow. A particular example is provided by patterns that are periodic in one variable and localized in the other spatial direction, for which our results in section 4 give excellent agreement with abstract theoretical predictions, primarily because we can represent the underlying PDE uniquely by a dynamical system in the unbounded variable. Fully localized patterns,

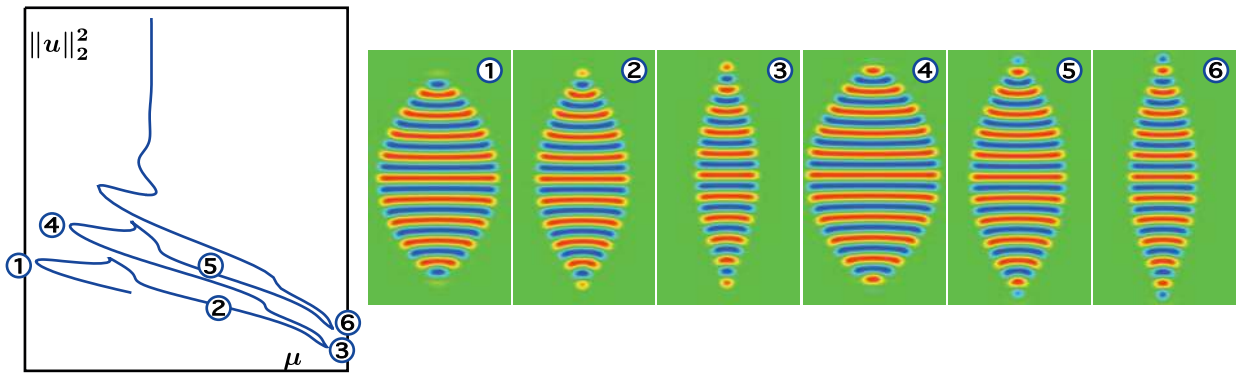

Figure 33. *The continuation results for $\nu = 2.46$ presented here illustrate how the curvature of the worm boundary near its peaked top and bottom end points changes along the solution branch: the sign of the curvature of the localized patterns in panels 3 and 6 near its peaked end points is different from those in the other panels. The family of worm profiles along the bifurcation curve can also be viewed in the accompanying movie file* (78274_02.mpg [3.9MB]). *The computation was done with $L_x = 88$, $L_y = 157$, $n_x = 257$, and $n_y = 1025$.*

on the other hand, may change in either of the two unbounded spatial variables as a parameter is varied, and there is no way of capturing these changes by a single spatial-dynamical system. Indeed, the fully localized hexagon patches studied in [31] exhibit a very complex bifurcation structure, with equally complex profile changes along their solution branch. The fully localized stripe patches that we considered in section 5 behave somewhere between these extremes, as the rolls they are comprised of select two distinct directions along which changes are preferred. The two different growth mechanisms in the direction along and transverse to the roll patterns are reflected in the spatial-dynamics interpretation we put forward in Figure 25, which, in turn, explained some of the features of worms we encountered during their numerical continuation.

However, these ideas cannot explain the precise shape of fully localized stripe patterns or the changes in curvature of the spatial interface between background and interior roll structures that are visible along the branch shown in Figure 33. These indicate that simple notions based on effective surface "tension" are insufficient to determine the shape of the structure, and suggest that the shape is defined by the competition between surface energy and changes in the bulk energy due to curvature-induced wavelength variation. Work along these lines includes that in [20], which used modulation equations to capture weakly nonlinear interfaces between a background and a hexagonal pattern in order to describe the possible shapes of the fully localized hexagonal structures computed in [31] for the planar Swift–Hohenberg equation. Similar structures are present in nonvariational systems as well [24], although for such systems energy-based methods are of doubtful value. A similar approach may be useful for elucidating the shape of worms, at least in the context of the planar Swift–Hohenberg equation. A possible alternative approach using Wulff diagrams, which are used to predict the shape of crystals through appropriate interfacial energies, may also be useful.

In most of our computations, fully localized stripe patterns cease to snake once their L^2-norm becomes large enough, although the results shown in Figure 30 are inconclusive in this regard. We speculate that worm branches will always stop snaking and instead approach a vertical asymptote, but have no proof to offer.

Finally, we mention the implications that our results may have for applications. Our computations for almost planar stripe patterns indicate that the asymmetric states created by the underlying bifurcation can be temporally stable. This is rather unexpected and raises, for instance, the possibility of finding stable asymmetric localized buckling modes of the cylindrical shells analyzed in [23]. Time-independent worm-like states of the type computed here should also be present in nonvariational systems such as convection with midplane reflection symmetry [4] or plane Couette flow [41], although their stability properties will differ.

REFERENCES

[1] H. Arbell and J. Fineberg, *Temporally harmonic oscillons in Newtonian fluids*, Phys. Rev. Lett., 85 (2000), pp. 756–759.

[2] Y. Astrov and Y. Logvin, *Formation of clusters of localized states in a gas discharge system via a self-completion scenario*, Phys. Rev. Lett., 79 (1997), pp. 2983–2986.

[3] D. Avitabile, *Computation of Planar Patterns and Their Stability*, Ph.D. thesis, Department of Mathematics, University of Surrey, Surrey, UK, 2008.

[4] O. Batiste, E. Knobloch, A. Alonso, and I. Mercader, *Spatially localized binary-fluid convection*, J. Fluid Mech., 560 (2006), pp. 149–158.

[5] M. Beck, J. Knobloch, D. J. B. Lloyd, B. Sandstede, and T. Wagenknecht, *Snakes, ladders, and isolas of localized patterns*, SIAM J. Math. Anal., 41 (2009), pp. 936–972.

[6] U. Bisang and G. Ahlers, *Bifurcation to worms in electroconvection*, Phys. Rev. E, 60 (1999), pp. 3910–3919.

[7] U. Bortolozzo, M. G. Clerc, and S. Residori, *Solitary localized structures in a liquid crystal light-valve experiment*, New J. Phys., 11 (2009), paper 093037.

[8] J. Burke and E. Knobloch, *Localized states in the generalized Swift-Hohenberg equation*, Phys. Rev. E, 73 (2006), paper 056211.

[9] J. Burke and E. Knobloch, *Homoclinic snaking: Structure and stability*, Chaos, 17 (2007), paper 037102.

[10] J. Burke and E. Knobloch, *Snakes and ladders: Localized states in the Swift-Hohenberg equation*, Phys. Lett. A, 360 (2007), pp. 681–688.

[11] A. R. Champneys and B. Sandstede, *Numerical computation of coherent structures*, in Numerical Continuation Methods for Dynamical Systems, B. Krauskopf, H. M. Osinga, and J. Galan-Vioque, eds., Springer, New York, 2007, pp. 331–358.

[12] S. J. Chapman and G. Kozyreff, *Exponential asymptotics of localized patterns and snaking bifurcation diagrams*, Phys. D, 238 (2009), pp. 319–354.

[13] P. Coullet, C. Riera, and C. Tresser, *Stable static localized structures in one dimension*, Phys. Rev. Lett., 84 (2000), pp. 3069–3072.

[14] J. D. Crawford and E. Knobloch, *Symmetry and symmetry-breaking bifurcations in fluid mechanics*, in Ann. Rev. Fluid Mech. 23, Annual Reviews, Palo Alto, 1991, pp. 341–387.

[15] M. Cross and P. Hohenberg, *Pattern formation outside of equilibrium*, Rev. Mod. Phys., 65 (1993), pp. 851–1112.

[16] H. Dankowicz and F. Schilder, *A new development platform for parameter continuation and bifurcation analysis in nonlinear dynamical systems*, in Proceedings of the 8th World Congress on Computational Mechanics (WCCM8), Venice, Italy, 2008.

[17] F. Daviaud, J. Hegseth, and P. Bergé, *Subcritical transition to turbulence in plane Couette flow*, Phys. Rev. Lett., 69 (1992), pp. 2511–2514.

[18] M. Dennin, G. Ahlers, and D. S. Cannell, *Chaotic localized states near the onset of electroconvection*, Phys. Rev. Lett., 77 (1996), pp. 2475–2478.

[19] E. J. Doedel and B. Oldeman, AUTO07P*: Continuation and Bifurcation Software for Ordinary Differential Equations*, Technical report, Faculty of Engineering and Computer Science, Concordia University, Montreal, 2009.

[20] D. Escaff and O. Descalzi, *Shape and size effects in localized hexagonal patterns*, Internat. J. Bifur. Chaos Appl. Sci. Engrg., 19 (2009), pp. 2727–2743.
[21] M. A. Heroux, R. A. Bartlett, V. E. Howle, R. J. Hoekstra, J. J. Hu, T. G. Kolda, R. B. Lehoucq, K. R. Long, R. P. Pawlowski, E. T. Phipps, A. G. Salinger, H. K. Thornquist, R. S. Tuminaro, J. M. Willenbring, A. Williams, and K. S. Stanley, *An overview of the Trilinos project*, ACM Trans. Math. Software, 31 (2005), pp. 397–423.
[22] R. B. Hoyle, *Pattern Formation*, Cambridge University Press, Cambridge, UK, 2006.
[23] G. W. Hunt, M. A. Peletier, A. R. Champneys, P. D. Woods, M. A. Wadee, C. J. Budd, and G. J. Lord, *Cellular buckling in long structures*, Nonlinear Dynam., 21 (2000), pp. 3–29.
[24] O. Jensen, V. O. Pannbacker, E. Mosekilde, G. Dewel, and P. Borckmans, *Localized structures and front propagation in the Lengyel–Epstein model*, Phys. Rev. E, 50 (1994), pp. 736–749.
[25] A. Joets and R. Ribotta, *Localized, time-dependent state in the convection of a nematic liquid crystal*, Phys. Rev. Lett., 60 (1988), pp. 2164–2167.
[26] J. Knobloch and T. Wagenknecht, *Homoclinic snaking near a heteroclinic cycle in reversible systems*, Phys. D, 206 (2005), pp. 82–93.
[27] P. Kolodner, *Coexisting traveling waves and steady rolls in binary-fluid convection*, Phys. Rev. E, 48 (1993), pp. R665–R668.
[28] G. Kozyreff and S. J. Chapman, *Asymptotics of large bound states of localized structures*, Phys. Rev. Lett., 97 (2006), paper 044502.
[29] K.-J. Lee, W. D. McCormick, J. E. Pearson, and H. L. Swinney, *Experimental observation of self-replicating spots in a reaction-diffusion system*, Nature, 369 (1996), pp. 215–218.
[30] O. Lioubashevski, Y. Hamiel, A. Agnon, Z. Reches, and J. Fineberg, *Oscillons and propagating solitary waves in a vertically vibrated colloidal suspension*, Phys. Rev. Lett., 83 (1999), pp. 756–759.
[31] D. J. B. Lloyd, B. Sandstede, D. Avitabile, and A. R. Champneys, *Localized hexagon patterns of the planar Swift–Hohenberg equation*, SIAM J. Appl. Dyn. Syst., 7 (2008), pp. 1049–1100.
[32] D. Peterhof, B. Sandstede, and A. Scheel, *Exponential dichotomies for solitary-wave solutions of semilinear elliptic equations on infinite cylinders*, J. Differential Equations, 140 (1997), pp. 266–308.
[33] S. Pirkl, P. Ribière, and P. Oswald, *Forming process and stability of bubble domains in dielectrically positive cholesteric liquid crystals*, Liquid Crystals, 13 (1993), pp. 413–415.
[34] L. M. Pismen, *Patterns and Interfaces in Dissipative Dynamics*, Springer-Verlag, Berlin, 2006.
[35] Y. Pomeau, *Front motion, metastability, and subcritical bifurcations in hydrodynamics*, Phys. D, 23 (1986), pp. 3–11.
[36] R. Richter and I. V. Barashenkov, *Two-dimensional solitons on the surface of magnetic fluids*, Phys. Rev. Lett., 94 (2005), paper 184503.
[37] H. Sakaguchi and H. R. Brand, *Stable localized solutions of arbitrary length for the quintic Swift-Hohenberg equation*, Phys. D, 97 (1996), pp. 274–285.
[38] B. Sandstede and A. Scheel, *Defects in oscillatory media: Toward a classification*, SIAM J. Appl. Dyn. Syst., 3 (2004), pp. 1–68.
[39] B. Sandstede and A. Scheel, *Relative Morse indices, Fredholm indices, and group velocities*, Discrete Contin. Dyn. Syst. Ser. A, 20 (2008), pp. 139–158.
[40] B. Schäpers, M. Feldmann, T. Ackemann, and W. Lange, *Interaction of localized structures in an optical pattern-forming system*, Phys. Rev. Lett., 85 (2000), pp. 748–751.
[41] T. M. Schneider, J. F. Gibson, and J. Burke, *Snakes and ladders: Localized solutions of plane Couette flow*, Phys. Rev. Lett., 104 (2010), paper 104501.
[42] N. Tillmark and P. H. Alfredsson, *Experiments on transition in plane Couette flow*, J. Fluid Mech., 235 (1992), pp. 89–102.
[43] L. N. Trefethen, *Spectral Methods in* MATLAB, Software Environ. Tools 10, SIAM, Philadelphia, 2000.
[44] P. B. Umbanhowar, F. Melo, and H. L. Swinney, *Localised excitations in a vertically vibrated granular layer*, Nature, 382 (1996), pp. 793–796.
[45] P. D. Woods and A. R. Champneys, *Heteroclinic tangles and homoclinic snaking in the unfolding of a degenerate reversible Hamiltonian-Hopf bifurcation*, Phys. D, 129 (1999), pp. 147–170.